

# Chapter 6

## Systematic Uncertainties and Corrections

### 6.1 Introduction

The  $P_\mu^\pi \xi$  uncertainties are summarised in Table 6.1. The entries will be described fully in the current chapter. The table lists *systematic* uncertainties that are unique to the polarisation at the time of decay; the other systematic uncertainties are determined simultaneously with the parameters  $\rho$  and  $\delta$ . The largest uncertainty is from the  $P_\mu$  simulation: the muon beam and magnetic field together determine the muon's polarisation at target entry, and our knowledge of these limited the accuracy of the final result. The table has two *statistical* uncertainties; these could be reduced by accumulating more data and/or simulation under the same running conditions.

There are four corrections to  $\Delta P_\mu^\pi \xi$  (the difference in  $P_\mu^\pi \xi$  between the data and a hidden simulation value):

1. The simulation does not include depolarisation of the muons while leaving the muon production target, resulting in a correction of  $+0.9 \times 10^{-4}$  to the nominal sets, and  $+5.9(5.2) \times 10^{-4}$  for the sets at  $\langle p \rangle = 28.75 \text{ MeV}/c$  ( $28.85 \text{ MeV}/c$ ). The uncertainty from these corrections is included in Table 6.1.
2. The simulations were generated with an incorrect rate for the time-dependent depolarisation. A correction is applied rather than re-generating the simulation, since this would require several months of computer processing. The correction is  $+2.9 \times 10^{-4}$  for silver (2006) and  $+2.4 \times 10^{-4}$  for aluminium (2007). The uncertainty of this correction is negligible.
3. The statistics in the simulation spectra exceed the data by a factor of 1.8 to 4.0, depending on the set. This introduces a very small bias in the central value of  $\Delta P_\mu^\pi \xi$  during the spectrum fitting (see Section 3.4 for a description of the fitting

technique). As a result, a set-independent correction of  $-0.5 \times 10^{-4}$  is applied. The uncertainty of this correction is  $\pm 0.5 \times 10^{-4}$ , which is too small to enter Table 6.1.

4. The excess statistics in the simulation also causes a bias in the energy calibration procedure. This is applied as a set-dependent correction of between  $+1.3 \times 10^{-4}$  and  $+2.3 \times 10^{-4}$ ; the exact numbers will be given in Chapter 7. The uncertainty of this correction is  $< 0.5 \times 10^{-4}$ , which is again too small to enter Table 6.1.

Corrections 1 and 2 will be described in this chapter. Further detail on corrections 3 and 4 can be found elsewhere[79, 97].

Table 6.1: Uncertainties for  $\Delta P_\mu^\pi \xi$ , the difference in  $P_\mu^\pi \xi$  between the data and a hidden simulation value. These are systematic unless marked (stat.).

Category	Section	$\Delta P_\mu^\pi \xi$ uncertainty ( $\times 10^{-4}$ )		
		This analysis	MacDonald '08 [10, 83]	Jamieson '06 [21, 57]
<b>Polarisation</b>				
Magnetic field map and $\mu^+$ beam	6.2.1 to 6.2.9	<b>-4.0,+15.8</b>	Not eval. <sup>a</sup>	34.0
Stopping material				
Systematic effects	6.2.10	<b>3.2</b>	Not eval.	12.0
$\lambda$ (stat.)	6.2.10	2.4	Not eval.	Not eval.
$\mu^+$ production target	6.2.11	0.3	Not eval.	2.1
Background muons	6.2.12	1.0	Not eval.	1.8
<b>Chamber response</b>				
DC space-time-relationship	6.3.1	0.9	6.0	Not eval.
DC geometric effects	6.3.2	1.3	0.7	2.2
US-DS efficiency	6.3.3	1.4	1.1	1.9
Crosstalk	6.3.4	0.5	Not eval.	Not eval.
Wire time offsets	6.3.5	0.8	0.4	8.9
<b>Detector alignment</b>				
$z$ length scale	6.4	0.0	0.7	2.2
$u/v$ width scale	6.4	0.2	0.2	Not eval.
<b>Positron interactions</b>				
$\delta$ -electron rate	6.5.1	0.1	1.4	2.9
Bremsstrahlung rate	6.5.1	0.5	0.03	
Outside material	6.5.2	0.4	0.6	0.2
<b>Resolution</b>	6.6	1.5	0.7	Not eval.
<b>Momentum calibration</b>				
Tracking B-field	6.7.1	0.3	1.1	0.9
Kinematic endpoint				
Model uncertainty	6.7.2	1.4	Not eval.	Not eval.
Propagation to bulk	6.7.2	0.5	0.01	1.6
<b>Beam stability</b>				
Muon beam intensity	6.8.1	0.3	0.2	1.8
<b>External</b>				
Radiative corrections	6.9.1	0.5	0.5	1.0
$\eta$ correlation	6.9.2	1.1	1.1	Not eval.
Extraction of $\Delta P_\mu^\pi \xi$ (stat.) <sup>b</sup>	7.1	2.5	3.7	6
<b>Total systematic</b>		<b>-6.3,+16.5</b>	-	38
<b>Total statistical</b>		<b>3.5</b>	-	6

<sup>a</sup> In the most recent TWIST analysis (MacDonald '08), the polarisation uncertainties were not re-evaluated since it was a measurement of only  $\rho$  and  $\delta$ .

<sup>b</sup> This includes the statistical uncertainty from the kinematic endpoint parameters (see Section 6.7.2).

## 6.2 Polarisation

### 6.2.1 Overview

The simulation transports the muon spin from the position of the TECs ( $z \approx -191$  cm) to the metal stopping target ( $z \approx 0$  cm). This relies on the accuracies of the muon beam measurement and the magnetic field map, both of which will contribute to the assessment of the  $P_\mu^\pi \xi$  uncertainty. The term “fringe field” will be widely used; this refers to the magnetic field from the end of the M13 beam line up to the first drift chamber.

The systematic uncertainties from the muon beam and fringe field are summarised in Table 6.2, in the order they appear in this chapter. First, the uncertainties in the alignment of the muon beam and the magnetic field map will be described. These will be used simultaneously to establish an uncertainty of  ${}_{-1.2}^{+6.4} \times 10^{-4}$ . Second, the uncertainties in the transverse magnetic field components will be evaluated using three consistency tests, and these will set an uncertainty of  ${}_{-0.0}^{+13.9} \times 10^{-4}$ . Third, uncertainty in the width of the muon beam angular distributions will lead to three uncertainties that total  $\pm 3.8 \times 10^{-4}$ .

Table 6.2: Summary of muon beam and fringe field uncertainties, for sets with a nominal beam tune.

Description	$\Delta P_\mu^\pi \xi$ uncertainty ( $\times 10^{-4}$ )
$\mu^+$ beam and magnetic field alignment	-1.2,+6.4
Magnetic field transverse components	-0.0,+13.9
$\mu^+$ beam angular distributions	
Simulation of multiple scattering	$\pm 3.1$
Noise from TEC electronics	$\pm 1.7$
Aging of TEC sense planes	$\pm 1.5$
<b>Quadratic sum</b>	<b>-4.0,+15.8</b>

---

## 6.2.2 Measures of polarisation

Throughout this chapter the muon beam’s polarisation is always considered to be an average of the  $z$ -components of the muons’ spins, *not* the average of the spin projected onto the momentum vector. Two measurements of polarisation will now be described<sup>36</sup>.

In the simulation, the absolute polarisation is available *before* any time-dependent target depolarisation has taken place. This is the polarisation after passing through the solenoidal magnetic field, and it is calculated by simply averaging the  $z$ -components of the muons’ spins. From here on the simulation’s absolute polarisation is written as  $P_\mu(0)$ , where the (0) is a reminder that it is effectively determined at  $t = 0$ . Since the simulation knows the spin of each muon exactly,  $P_\mu(0)$  is known with high precision using a relatively small number of muons.

A fit between two decay positron spectra (data or simulation) measures  $\Delta P_\mu^D \xi$ , where  $P_\mu^D$  is the decay polarisation of the muon *after* time-dependent depolarisation has taken place. If the spectra have the same  $\xi$  and time dependence, then this quantity is directly comparable to changes in  $P_\mu(0)$ . Spectrum fits between the data with a nominal and steered beam will later be used to evaluate the leading systematic uncertainty for this measurement.

## 6.2.3 Initial beam position and angle alignment

A muon beam measurement was made with the TECs at the beginning and end of most data sets. These two measurements have small differences in position and angle, resulting in different values of  $P_\mu(0)$ . Since the GEANT simulation can only use one of the beam measurements, the differences must be assessed as a systematic uncertainty.

The changes in average position and angle between the two muon beam measurements are listed in Table 6.3, where differences of up to 0.18 cm in position and 3 mrad in angle are observed. Note that these changes are smaller than the observations from the previous TWIST  $P_\mu^\pi \xi$  analysis. The cause of the changes could be muon beam instability, a variation in the TEC drift cell response, or a limitation in the reproducibility of the position and angle of the TECs. Each of these possible causes will now be discussed.

Muon beam instabilities could originate from an instability in the M13 beam line

---

<sup>36</sup>A third measurement is possible using the time dependence of the forward-backward asymmetry. This was described in Section 3.6:  $P_\mu(t) = P_\mu^*(0) \exp(-\lambda t)$  is fit to the asymmetry. The difference in  $P_\mu^*(0)$  between two data sets is then a measure of their polarisation difference, as long as  $\lambda$  is the same for each set. Polarisation differences from  $P_\mu^*(0)$  are *not* used in this chapter.

Table 6.3: Muon beam differences for the beginning and end of set TEC measurements. The temperature difference between the measurements is denoted by  $\Delta T$ .

Set	Target	Description	$\Delta \langle x \rangle$ (cm)	$\Delta \langle y \rangle$ (cm)	$\Delta \langle \theta_x \rangle$ (mrad)	$\Delta \langle \theta_y \rangle$ (mrad)	$\Delta T^a$ ( $^{\circ}\text{C}$ )
68	Ag	Stopping distrib. peaked $\frac{1}{3}$ into target	0.11	-0.05	0.2	-3.2	-0.3
70	Ag	B = 1.96 T	0.03	0.00	1.0	-0.4	-1.2
71	Ag	B = 2.04 T	0.09	-0.05	0.0	0.1	2.4
74	Ag	Nominal A <sup>b</sup>	-	-	-	-	-
75	Ag	Nominal B	0.04	-0.10	-0.5	1.5	3.2
76	Ag	Steered beam	-0.04	-0.06	-0.6	1.9	1.3
83	Al	Downstream beam package in place	0.12	-0.09	0.6	0.7	-0.3
84	Al	Nominal C	0.18	-0.15	0.2	1.4	-0.4
86	Al	Steered beam B	0.04	-0.01	1.0	-0.01	-0.4
87	Al	Nominal D	0.13	-0.11	-0.1	0.7	-1.3
91/92/93	Al	Lower momentum <sup>b</sup>	-	-	-	-	-

<sup>a</sup>  $\Delta T = T_{\text{end}} - T_{\text{start}}$ , so that  $\Delta T > 0$  indicates a temperature rise between measurements.

<sup>b</sup> These sets only had one TEC measurement.

elements (*i.e.* quadrupoles, dipoles, slits, jaws, asymmetric currents for quadrupole steering), or a change in the proton beam upstream of the muon production target. We do not believe there were measurable M13 beam line instabilities since all elements were monitored with a slow control system, and runs where an element fluctuated were not analysed (see Section 5.4). The proton beam was ruled out as a significant source of instability. In detail, a special test was carried out with the proton beam displaced at the production target by  $\pm 0.1$  cm vertically, which is about five times larger than the beam could have moved during normal operation<sup>37</sup>. For this test, the largest observed TEC changes in the muon beam were  $\Delta \langle y \rangle = \pm 0.07$  cm in position and  $\Delta \langle \theta_y \rangle = \pm 1.0$  mrad in angle, which are negligible after scaling down by a factor of five.

We have good evidence that the muon beam was sufficiently stable throughout a set, and was therefore not the cause of the variations in Table 6.3. First, we acquired a whole week of data with the TECs in place throughout (set 72), and found that the average muon beam position and angle were stable to  $< 0.02$  cm and  $< 1$  mrad, respectively (see

<sup>37</sup>The proton beam was surrounded by four monitor plates (top, bottom, left, right). In order to steer the beam vertically by 0.1 cm and avoid destroying the top or bottom plate, the proton beam current was reduced from the nominal setting of  $\approx 100 \mu\text{A}$  to  $\approx 20 \mu\text{A}$ . This suggests that during normal operation the proton beam could not have moved by more than  $\approx 20/100 \times 0.1 \text{ cm} = 0.02 \text{ cm}$ .

---

Fig. 5.2). Second, when the TECs were not in place the muon beam measurement from the wire chambers was used to monitor the beam's stability; a typical monitoring plot was shown in Fig. 5.3. The sensitivity of this measurement was calibrated by deliberately changing the currents in each quadrupole and dipole by  $\pm 5\%$ . This allowed us to conclude that the muon beam instabilities that were observed are all small and uncorrelated with any beginning/end of set changes in Table 6.3.

The space-time-relationship (STR) in the TEC drift cells depended on temperature. This was ruled out as the cause of the differences in Table 6.3. In detail, new STRs were prepared that corresponded to a  $\pm 3^\circ\text{C}$  variation, and all the data from the TECs were then re-analysed. The average reconstructed positions changed by between 0.028 cm and 0.050 cm, depending on the proximity of the beam to the sense plane of the TEC<sup>38</sup>. The predicted changes in angle were all  $< 0.05$  mrad, except for set 76, which was still predicted to change by only 0.4 mrad. Clearly these changes in position and angle cannot explain the larger differences observed in Table 6.3.

Lastly, the insertion and removal of the TECs required the beam line elements to be switched off, and a breaking of the vacuum in the beam line, which then had to be pumped down again before data could be taken with the TECs. This process exerted significant forces on the beam line components and the box containing the TECs, and these forces are the prime candidate for the measured variation in initial position and angle. Therefore we conclude that the muon beam itself was stable and no systematic uncertainty is necessary for its fluctuations. Instead an uncertainty from the initial position and angle of the muon beam is needed, since we cannot be sure that the alignment of the TECs was reproducible.

Later we will evaluate the  $P_\mu(0)$  sensitivity to position changes of  $\pm 0.2$  cm and angle changes of  $\pm 3$  mrad. These are the limits of the observations in Table 6.3, but they are not overly conservative for a number of reasons. First, there are not enough entries in Table 6.3 to establish whether the changes in position and angle follow a predictable distribution. Second, the TECs were aligned to the drift chambers with a systematic uncertainty of about 2 mrad. And third, the long-term stability measurements of the TECs found movements of 0.1 cm, but they only had an accuracy of about 0.1 cm (see Section 2.13 for more information on the alignments and stability measurements).

---

<sup>38</sup>The  $x$ -positions increased with temperature and the  $y$ -positions decreased; see Ref. [76] for further detail.

## 6.2.4 Magnetic field position and angle alignment

The fringe field map for the analysis was generated with the `Opera` software package[85]. The generated map was compared to  $B_z$  measurements that were taken with Hall probes (see Appendix D). This comparison could not produce a precise translational alignment in  $x$  and  $y$ . Instead the position of the muon beam inside the detector was used. On a set-by-set basis, a field translation was determined such that the data and simulation positions matched. On average this required a translation of the entire map by<sup>39</sup>  $(\Delta x, \Delta y) = (0.21, 0.15)$  cm. The uncertainties in this translation from the muon beam and an error in the strength of the magnetic field components were evaluated, and found to be  $\pm 0.04$  cm. This is smaller than the uncorrelated uncertainty from the Hall probe alignment; these were aligned in the yoke's coordinate system system to  $< 0.1$  cm in  $x$  and  $y$  and  $< 1$  mrad in  $\theta_x$  and  $\theta_y$ [98]. The next section will use the uncorrelated uncertainties from the Hall probe alignment to determine the systematic uncertainty for  $P_\mu(0)$ .

## 6.2.5 Alignment uncertainties from beam and magnetic field

Section 6.2.3 established that the alignment of the muon beam is uncertain at the level of  $\pm 0.2$  cm in both the  $x$  and  $y$  position, and  $\pm 3$  mrad in both the  $\theta_x$  and  $\theta_y$  position. Similarly, Section 6.2.4 established the alignment of the magnetic field map to be uncertain at the level of  $\pm 0.1$  cm in  $x$  and  $y$ , and  $\pm 1$  mrad in  $\theta_x$  and  $\theta_y$ . All of these uncorrelated uncertainties must be combined in order to determine the sensitivity of  $P_\mu(0)$  to possible misalignments.

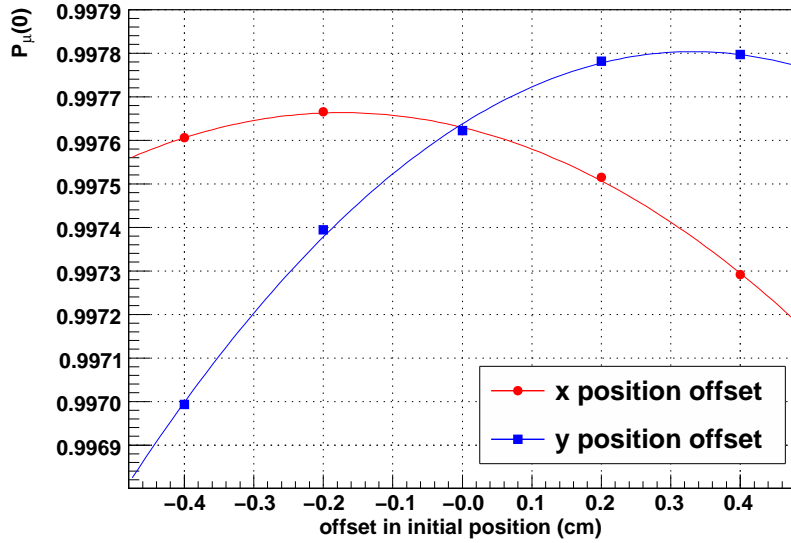
The dependence of  $P_\mu(0)$  on each alignment is non-linear. This is demonstrated for a nominal beam in Fig. 6.1. In addition, since the experimental beam is optimised with respect to the solenoid axis, the quantity  $P_\mu(0)$  is also optimised, and introducing a combination of misalignments is therefore more likely to reduce  $P_\mu(0)$  than increase it. As a result of these complications, the uncertainties are combined using a Monte Carlo approach. One hundred simulations are run with each misalignment selected from an independent Gaussian distribution with the standard deviation equal to the alignment uncertainty. For example, the initial beam position in  $x$  is drawn from a Gaussian with a mean of 0.0 cm, and standard deviation equal to 0.2 cm. The resulting  $P_\mu(0)$  distribution

---

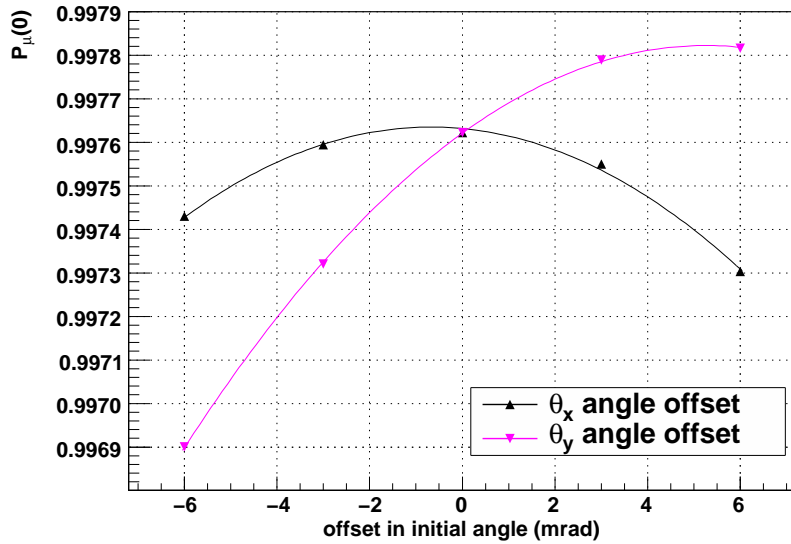
<sup>39</sup>In practice, an early analysis found a preliminary translation of  $(\Delta x, \Delta y) = (0.20, 0.20)$  cm, and this was used to generate all the simulations. The correction between the preliminary translation of  $(\Delta x, \Delta y) = (0.20, 0.20)$  cm and the final value of  $(\Delta x, \Delta y) = (0.21, 0.15)$  cm was evaluated to have a negligible effect on  $P_\mu(0)$  ( $< 0.6 \times 10^{-4}$  for the nominal sets.)

---

from these simulations is asymmetric, and the width above and below the central value is used to establish a  $P_\mu(0)$  systematic uncertainty of  ${}_{-6.4}^{+1.2} \times 10^{-4}$  for the nominal sets. The uncertainty for  $\Delta P_\mu^\pi \xi$ , the difference between the data and a hidden simulation value, is then  ${}_{-1.2}^{+6.4} \times 10^{-4}$ .



(a) Initial position sensitivity.



(b) Initial angle sensitivity.

Figure 6.1: The polarisation of the muons after the fringe field,  $P_\mu(0)$ , has a quadratic dependence on changes in the initial position and angle of the beam. The results of simulating a nominal beam profile (set 74) are shown.

## 6.2.6 Overview of the magnetic field map

The magnetic field map for the analysis was generated using the `Opera` software package[85]. The resulting components of  $\vec{B}$  are shown in Figs. 6.2 and 6.3. The longitudinal components ( $B_z$ ) increase steadily up to the drift chamber (DC) tracking region. The transverse components ( $B_x$ ,  $B_y$ ) are less than 1.5 mT while on-axis ( $x = y = 0$ ), but increase significantly off-axis; Fig. 6.3(a) demonstrates this by including the components for ( $x = y = 1$  cm). The transverse components have approximate radial symmetry and are maximised just inside the door of the yoke. They are also strongly linear within  $\approx 5$  cm of the axis, which fully encloses the volume through which the muons pass (see Fig. 6.3(c)). The transverse components are closely related to the depolarisation, which is shown for the simulation of a nominal profile in Fig. 6.3(b). For example, the onset of rapid depolarisation coincides with the maximisation of the transverse components, and the field's inflection at  $z = -100$  cm is accompanied by an inflection in the depolarisation. Clearly the quality of the fringe field downstream of the door is important since it controls the rate of depolarisation. In addition, the field upstream of the door must be known since it affects the part of the fringe field which the beam is transported through.

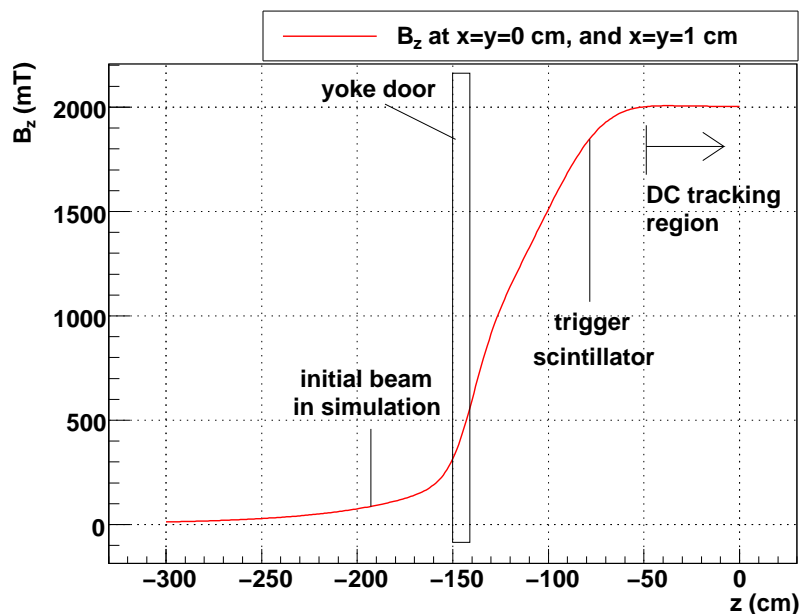
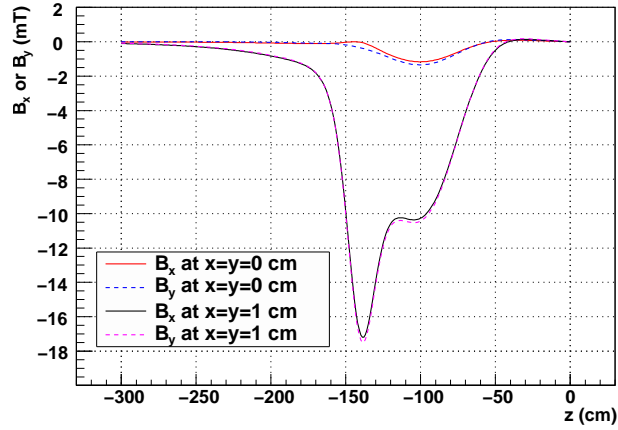
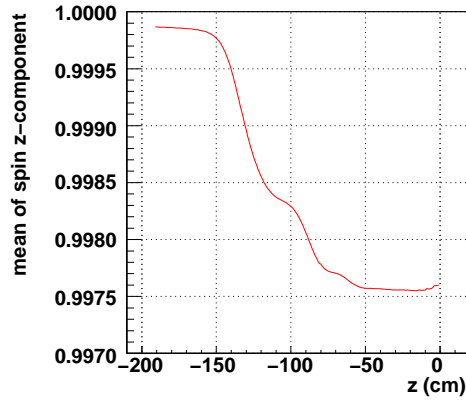


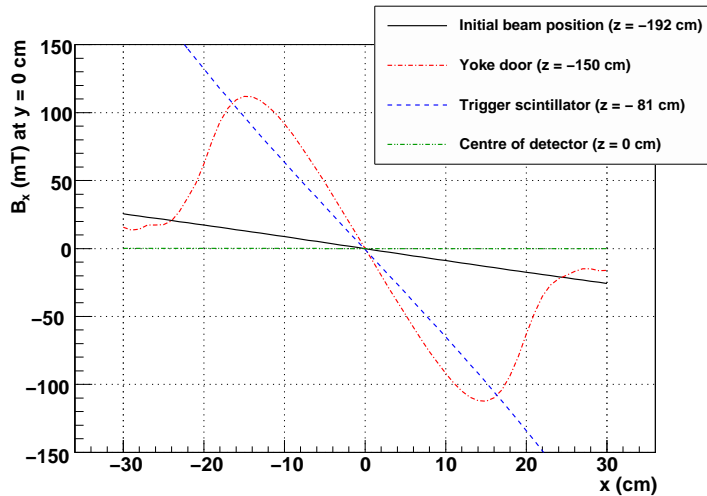
Figure 6.2: Longitudinal ( $B_z$ ) components from the field map used for the analysis. These are produced from an `Opera` finite element analysis[85].



(a)  $B_x$  and  $B_y$  components.



(b) Average of spin  $z$ -component, for a nominal beam profile.



(c)  $B_x$  components for  $y = 0$  cm.

Figure 6.3: Transverse fringe field components,  $B_x$  and  $B_y$ , from the field map used for the analysis. The average spin is also shown since its behaviour is closely related to the transverse components.

---

The  $B_z$  components from `Opera` are compared to Hall probe measurements in Fig. 6.4, where discrepancies of up to 6 mT are observed. The same comparison is not possible for the smaller  $B_x$  and  $B_y$  components since the Hall probes were single axis and did not measure them. We have identified three possible causes for the discrepancies. First, the `Opera` software did not include all the boundary conditions, such as the steel in the floor of the M13 area and the final M13 quadrupoles; an attempt was made to include these quadrupoles, but it did not find a significant effect for the  $B_z$  components. Second, there were several inputs to `Opera` that had to be tuned within their measured accuracy. For example, adjustments were made to the solenoid’s coil positions in  $x/y/z$ , the radii of these coils and their current densities, the  $B - H$  curve for the iron yoke, and the position of the yoke door in  $z$ [99, 100, 101, 102]. There was freedom of up to 0.2 cm in the positions of the solenoid coils[99], since their positions were not measured, and were instead initially placed according to a sketch from the magnet manufacturer. The previous  $P_\mu^\pi \xi$  measurement found that variations in the `Opera` inputs affected  $P_\mu(0)$  by  $3 \times 10^{-4}$  at most[57]. As a result of this low sensitivity the `Opera` inputs were not tuned further for the current measurement. Third, the `Opera` software used a finite element method to solve Maxwell’s equations. This is expected to have limitations when modelling the 40 cm diameter circular hole in the yoke door at  $z = -150$  cm, which is at a critical region for the *transverse* field components and hence the depolarisation. This is because there are several orders of length scale involved, and it is reasonable to expect that finite element analyses will suffer from accuracy problems under these conditions. In this case, the muons are within  $\lesssim 5$  cm of the axis, there is a circular hole in the yoke of diameter 40 cm, and the whole map must be determined over a  $z$ -length of about 5 m.

If the discrepancy in the  $B_z$  components is eliminated, then the  $P_\mu(0)$  estimates are changed by  $< 1 \times 10^{-4}$  for all profiles; this test does not obey Maxwell’s equations, but it does demonstrate that a discrepancy of a few mT in only the  $B_z$  components is unimportant at the  $10^{-4}$  level. In contrast, a change of a few mT in the  $B_x$  and  $B_y$  components has a significant effect on  $P_\mu(0)$ . Since there are no Hall probe measurements of the  $B_x$  and  $B_y$  components, the uncertainty from them must be evaluated indirectly. We carry out this evaluation by comparing how well the simulation reproduces large differences in polarisation between sets with a nominal and a steered muon beam. The next sections will describe this technique.

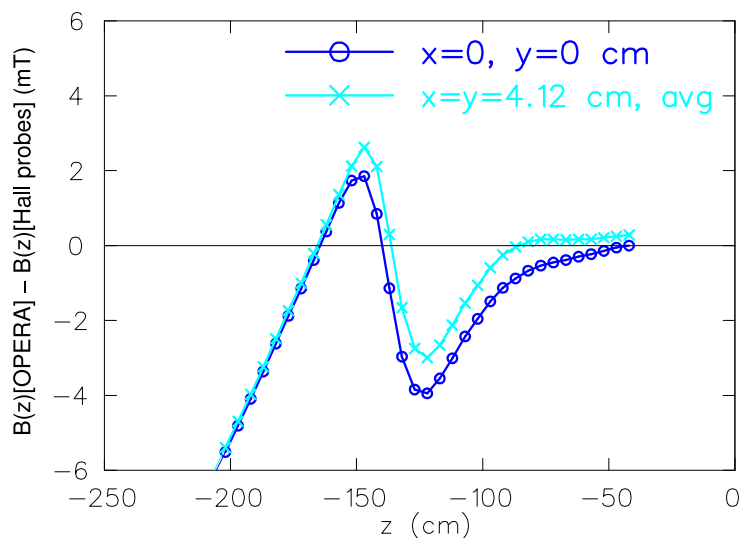


Figure 6.4: Difference in  $B_z$  between the magnetic field maps from Opera and the Hall probes. Two comparisons are shown: on-axis ( $x = y = 0$ ) and an off-axis average of  $x = \pm 4.12$  cm,  $y = \pm 4.12$  cm. Note that muons start in the simulation at  $z = -191.944$  cm, and stop in the target at  $z = 0$  cm.

### 6.2.7 Muon beam tunes for evaluating the uncertainty

The nominal beam tune was described in Section 5.2; initially the position of the beam at the time expansion chambers (TECs) was steered to be close to  $x = y = 0$ , with the angles  $\theta_x$  and  $\theta_y$  minimised, but ultimately the tune was chosen to place the muon beam spots within the detector along a straight line, corresponding to minimised transverse momentum. The “envelope” of a simulated nominal muon beam, defined as the mean plus or minus one standard deviation, is shown in Figs. 6.5(a) and 6.5(b). Most of the beam remains within 1.0 cm of the solenoid’s axis, and is focussed by the field to a few millimetres in extent at  $z = -100$  cm. After this focus the envelope develops oscillations in its mean position and size.

Three additional beam tunes are shown in Fig. 6.5. These will be used to assess the systematic uncertainties for the fringe field. They are set 76, where the muon beam was steered to have  $\langle \theta_y \rangle \approx 28$  mrad at the TECs, set 86, where the beam was positioned off-axis and pointed away from the axis ( $\langle x \rangle \approx -1.0$  cm,  $\langle \theta_x \rangle \approx -10$  mrad), and set 72 where the TECs were in place throughout, which increased the muon beam’s emittance due to the additional multiple scattering. In the range where rapid depolarisation takes place, ( $-150 < z < -100$ ) cm, the beams for sets 76 and 86 sample the fringe field at

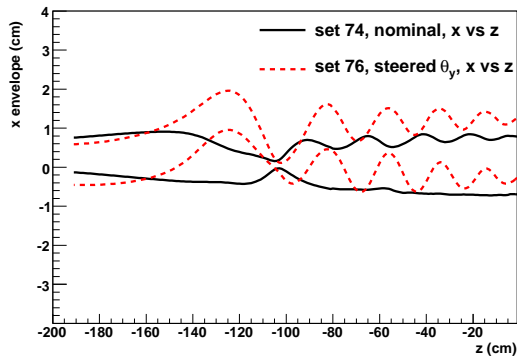
a different location to the nominal beam, with a non-zero average angle. They undergo a considerable focus, corresponding to an intersection of the field lines at a steep angle. As a result, these beams will be seen to undergo significantly more depolarisation, and the ability of the simulation to reproduce the depolarisation observed in the data will provide a stringent test of the fringe field model; such a validation was not available for the previous TWIST  $P_\mu^\pi \xi$  analysis.

The three pairs of sets are listed in Table 6.4, and from here-on they are labelled as comparisons I, II and III. The first column in Table 6.4 shows the differences in polarisation from data. These are determined by fitting the nominal and steered decay spectra against each other, and the uncertainties are purely statistical. The next column in Table 6.4 shows the simulation’s prediction for the polarisation difference using the Opera magnetic field map. These are evaluated using a Monte Carlo technique that is similar to Section 6.2.5. For each Monte Carlo trial, the initial position and angle of the beam are selected independently for the nominal and steered set, since we believe that variations originate from the reproducibility of the TECs. In contrast, the magnetic field position and angle must be the same for a nominal and steered set, so the same random values are used for both sets in each Monte Carlo trial.

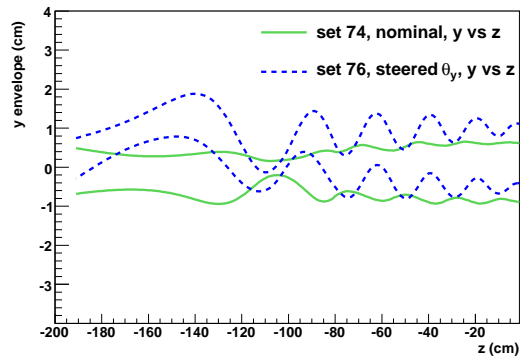
In terms of standard deviations, the simulation is seen to *underestimate* the depolarisation by  $2.0\sigma$  and  $0.6\sigma$  for comparisons I and II, and to *overestimate* the depolarisation by  $1.0\sigma$  for comparison III. The result for comparison I would not usually be a cause for concern; however, there is good reason to believe that an additional systematic uncertainty from the  $B_x$  and  $B_y$  components is missing.

Table 6.4: Validation of the fringe field map by establishing how well the simulation reproduces large polarisation differences in the data. Ideally the value of simulation minus data should be consistent with zero.

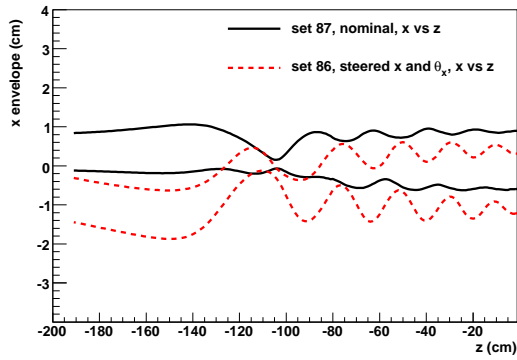
Comparison	Sets	Difference in polarisation ( $\times 10^{-4}$ )		
		Data	Simulation	Simulation minus data
I	74,76 (steered in $\theta_y$ )	$105 \pm 9$	$56_{-18}^{+23}$	$-48_{-20}^{+24}$
II	87,86 (steered in $x, \theta_x$ )	$62 \pm 8$	$47_{-16}^{+23}$	$-15_{-18}^{+24}$
III	74,72 (TECs-in)	$18 \pm 9$	$28_{-5}^{+12}$	$+10_{-10}^{+15}$



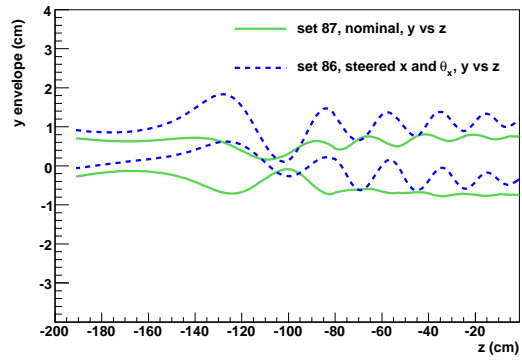
(a)



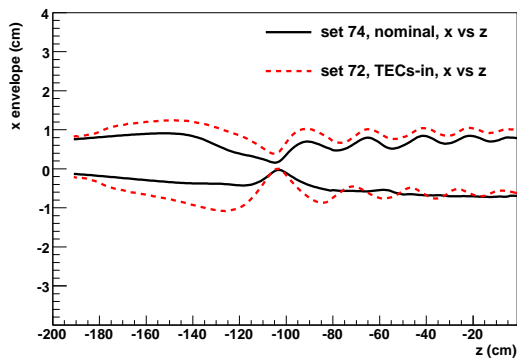
(b)



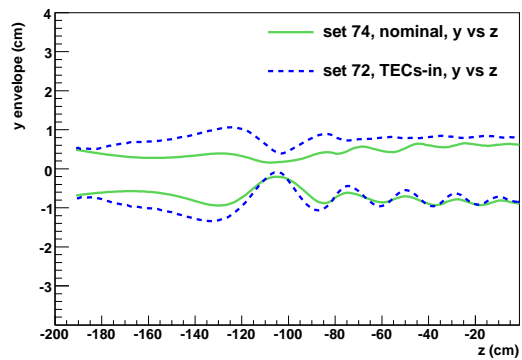
(c)



(d)



(e)



(f)

Figure 6.5: Muon beam *envelopes* from the simulation. These are defined as the mean position plus or minus one standard deviation.

Figures 6.3(a) and 6.3(c) show how the transverse field components depend on position. The muons are confined to within  $< 5$  cm of the axis, and Fig. 6.3(c) indicates that the field has a linear dependence on  $x$  (and  $y$ ) over this range. It is reasonable to expect that Opera has the correct linear shape, but may suffer from errors in the magnitude of the components. The sensitivity of comparison I to a scaling of  $B_x$  and  $B_y$  by a common factor,  $f$ , is shown in Fig. 6.6. The discrepancy of  $2.0\sigma$  between data and simulation can be reduced by increasing  $f$ , which increases the central value of the simulation, and enlarges the uncertainties in  $P_\mu(0)$  from alignments.

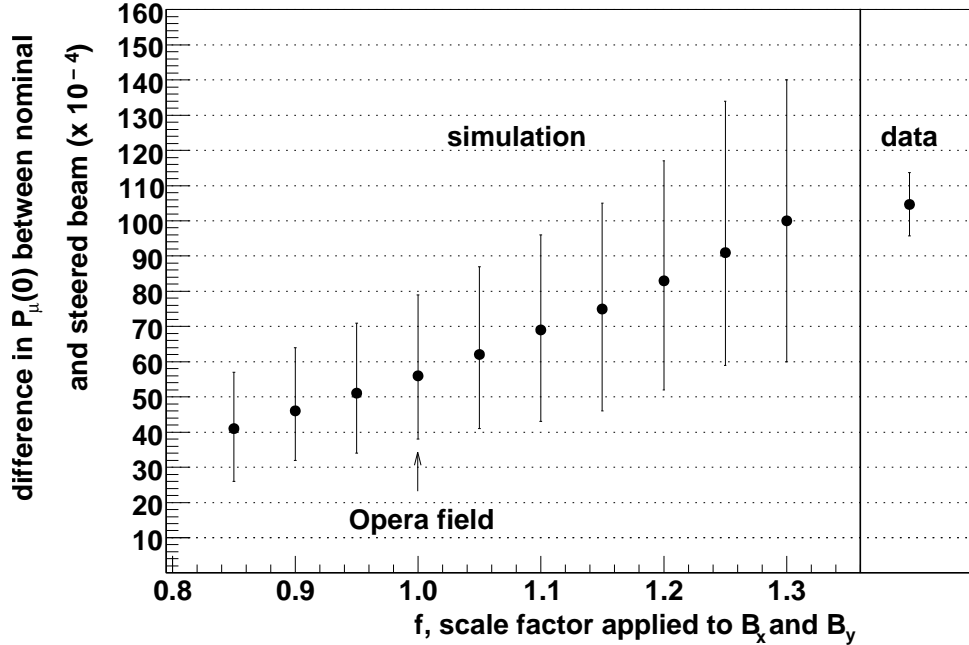


Figure 6.6: Comparison I is shown. With the original Opera field ( $f = 1.0$ ) the data and simulation differ by about two standard deviations. The agreement improves as the  $B_x$  and  $B_y$  components are scaled by a factor,  $f$ .

The systematic uncertainty is evaluated by considering the effect of the scaling,  $f$ , on all three comparisons. The number of standard deviations by which data and simulation differ is shown in Fig. 6.7(a), as  $f$  is varied. A decrease in the transverse field components is limited by comparison I, since the simulation rapidly diverges from the data as  $f$  is decreased. Similarly, an increase in the transverse field components is limited by comparison III.

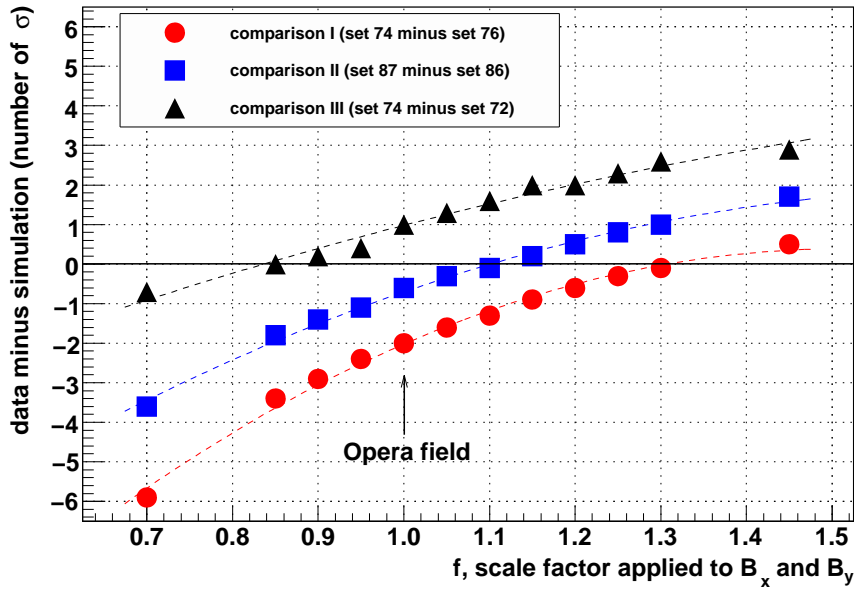
We have no reason to favour one of the comparisons over the others. Therefore we combine the differences between data and simulation for each comparison, and seek to

minimise this combination by scaling the transverse field components. Specifically the  $\chi^2$  statistic is calculated as

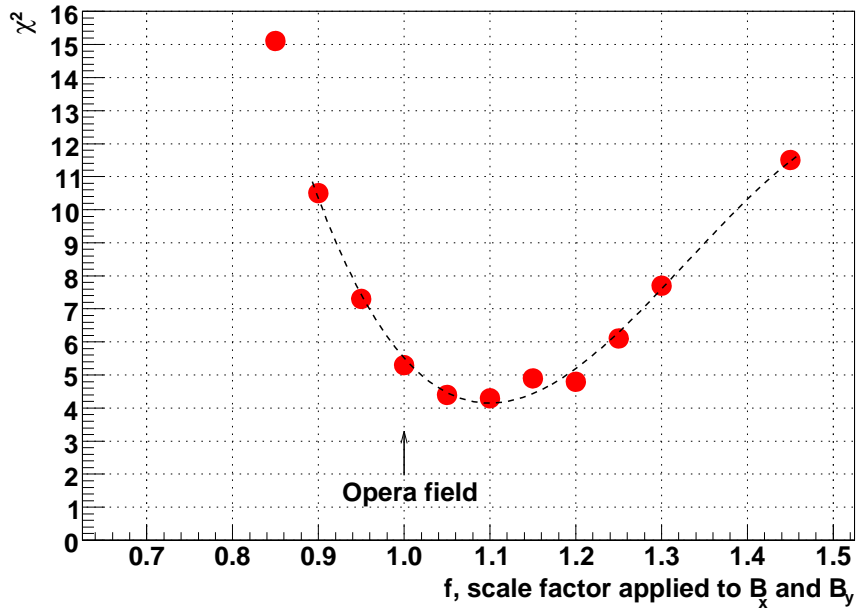
$$\chi^2 = \sum_{\text{comparisons}} \frac{(\bar{x}_{\text{data}} - \bar{x}_{\text{simulation}})^2}{\sigma_{\text{data}}^2 + \sigma_{\text{simulation}}^2} \quad (6.1)$$

where for convenience the definition  $x = \Delta P_\mu(0)$  has been made, and  $\Delta P_\mu(0)$  is the difference in polarisation between a nominal and a steered set. The resulting  $\chi^2$  statistic is shown in Fig. 6.7(b); a minimisation occurs when the transverse field components are scaled by  $f = 1.10$ . A correction of the result to this minimum is *not* made, since we cannot prove that the deviations between the **Opera** and true fields are fully covered by a simple scaling of the  $B_x$  and  $B_y$  components. Instead the  $f$  range corresponding to  $(\chi_{\text{minimum}}^2 + 1)$  is taken to present a reasonable maximum of our error due to not measuring the transverse field components. This leads to a range in  $f$  of 1.01 to 1.20. All nominal sets are evaluated at these two  $f$ -values, and the average difference in  $P_\mu(0)$  is  $13.9 \times 10^{-4}$ . This is assigned as a one sided uncertainty for  $P_\mu(0)$  of  ${}^{+0.0}_{-13.9} \times 10^{-4}$ . The uncertainty for  $\Delta P_\mu^\pi \xi$ , the difference between the data and a hidden simulation value, is then  ${}^{+13.9}_{-0.0} \times 10^{-4}$ .

We note that early studies used a different field map to investigate the systematic uncertainty from the magnetic field. Three on-axis coils were added to the original **Opera** map, and their currents were tuned to almost completely eliminate the  $B_z$  mismatch in Fig. 6.4. The coils also increased the  $B_x$  and  $B_y$  components, and the effect on the nominal set polarisation was  $14.1 \times 10^{-4}$ , on average. This is very close to the result derived from the simple scaling approach.



(a) Data-simulation agreement for all three comparisons.



(b) Combining the three comparisons into a  $\chi^2$ .

Figure 6.7: The transverse magnetic field components ( $B_x$  and  $B_y$ ) are multiplied by a factor,  $f$ . The difference in polarisation between a nominal and a steered set is sensitive to  $f$ . An overall better agreement is possible with  $f = 1.1$ , corresponding to a 10% increase in the strength of the transverse components.

## 6.2.8 Muon beam angular distribution width

The muons were multiple scattered as they passed through the TECs, resulting in a measured angle distribution that is larger than the distribution in the absence of the TECs. A GEANT3 simulation of the TECs finds that the root mean square of the angles should be reduced by a factor of  $c_x = 0.64$  in the  $x$ -module, and  $c_y = 0.48$  in the  $y$ -module to account for this multiple scattering. The correction in the  $y$ -module is larger since it is located downstream of the  $x$ -module. The dependence of  $P_\mu(0)$  on the choice of  $c_x$  is shown in Fig. 6.8 for a nominal and a steered beam. To an acceptable approximation,  $dP_\mu(0)/dc_x$  and  $d^2P_\mu(0)/dc_x^2$  are independent of the beam steering. For example, if  $c_x = 0.64$  then a variation of  $\pm 10\%$  in  $c_x$  changes  $P_\mu(0)$  by  $\frac{-1.8}{+2.1} \times 10^{-4}$  for the nominal case, and  $\frac{-1.9}{+2.0} \times 10^{-4}$  for the steered beam. As a result, the choice of  $c_x$  and  $c_y$  has no bearing on the comparison of polarisation differences between data and simulation, and the systematic uncertainties from these factors can be treated as orthogonal to those already evaluated.

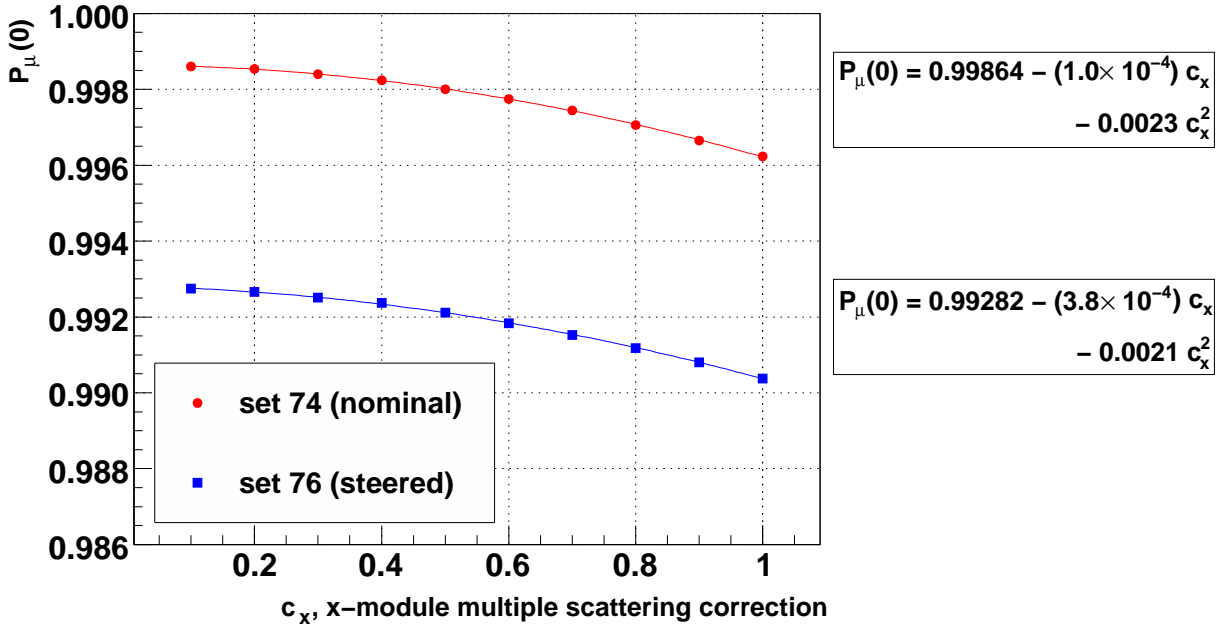


Figure 6.8: Sensitivity of the simulation's  $P_\mu(0)$  to  $c_x$ , the multiple scattering correction factor in the  $x$ -module. The ratio  $c_x/c_y = 0.64/0.48$  was maintained.

Note that although the simulation predicts the systematic uncertainties in this section are asymmetric, this asymmetry is at the  $10^{-5}$  level, which is too small to be significant; the systematic uncertainties are therefore quoted as *symmetric*, with the magnitude set

to the average of the upper and lower bounds.

The parameters  $c_x$  and  $c_y$  relied on the accuracy of multiple scattering in **GEANT3**. The author is unaware of any validation studies for the multiple scattering of muons with  $p \approx 30 \text{ MeV}/c$  in thin materials (the entire TEC apparatus was equivalent to just  $\approx 7 \text{ mg}/\text{cm}^2$  of material). Our most direct test of the **GEANT3** accuracy used five runs with the upstream window on the TECs changed from the nominal  $6 \mu\text{m}$  of Mylar to a thicker  $25 \mu\text{m}$  ( $3.2 \text{ mg}/\text{cm}^2$ ) window. The additional  $19 \mu\text{m}$  of material increased the scattering distribution so that<sup>40</sup>

$$\theta_{\text{TECs}+25 \mu\text{m}} \approx \sqrt{\theta_{\text{TECs}+6 \mu\text{m}}^2 + \theta_{19 \mu\text{m}}^2}. \quad (6.2)$$

The results for  $\theta_{19 \mu\text{m}}$  from data and simulation are shown in Table 6.5, where the simulation overestimates the root mean square width of the scattering distributions by 18.3% in the  $x$ -module and 15.6% in the  $y$ -module. This implies that the  $c_x$  and  $c_y$  factors were reliable to 17.0% (the average of the overestimate in each module), which results in a systematic uncertainty of  $\pm 3.1 \times 10^{-4}$ . The observed discrepancy of 17.0% must not be taken as a formal validation of multiple scattering in **GEANT3**, since there are systematic uncertainties associated with the values in Table 6.5 that have not been evaluated.

Table 6.5: Width of reconstructed angle distributions for Mylar windows of thickness  $6 \mu\text{m}$  and  $25 \mu\text{m}$ . These are placed on the upstream window of the TEC gas box. The bracketed number indicates the statistical uncertainty in the final digit.

Mylar window thickness ( $\mu\text{m}$ )	RMS of $\theta_x$ (mrad)		RMS of $\theta_y$ (mrad)	
	data	simulation	data	simulation
6	14.50 (5)	14.10 (7)	19.79 (7)	19.89 (6)
25	17.25 (8)	17.90 (9)	22.01 (6)	22.8 (1)
$\Rightarrow 19$	<b>9.3 (2)</b>	<b>11.0 (2)</b>	<b>9.6 (2)</b>	<b>11.1 (2)</b>

The TEC analysis code was reviewed for this measurement, and the accuracy of the reconstruction algorithm was found to be limited by noise from the electronics. This did not affect the mean position/angle, only the width of the angular distributions. An attempt to overcome this limitation resulted in two variants of the algorithm that are systematically different (see Appendix G.3.4). Since an event-by-event investigation could not distinguish which variant was the most accurate, the systematic difference between

<sup>40</sup>The multiple scattering distribution is non-Gaussian, and adding the widths of layers in quadrature will systematically underestimate the total width[3]. However, in this case we are comparing data and simulation where the same error is made in both.

the two is taken as a systematic uncertainty. For all sets this difference in  $P_\mu(0)$  was less than  $1.7 \times 10^{-4}$ , except for set 76 (steered) where  $P_\mu(0)$  changed by  $6.3 \times 10^{-4}$  between the two variants of the algorithm. A conservative systematic uncertainty of  $\pm 1.7 \times 10^{-4}$  is assigned for the nominal sets.

The width of the angular distributions depended on the mean number of hits in the final track ( $\langle n_x \rangle$  in the  $x$ -module,  $\langle n_y \rangle$  in the  $y$ -module), which decreased depending on the length of time that the sense planes were exposed to the beam. The same  $c_x$  and  $c_y$  correction factors were used for all muon beam measurements, despite differences in the age of the planes, and this resulted in a systematic uncertainty. The values of  $\langle n_x \rangle$  and  $\langle n_y \rangle$  for each set are shown in Fig. 6.9. The  $c_x$  and  $c_y$  factors were tuned using set 75, which had  $\langle n_x \rangle = 15.0$  and  $\langle n_y \rangle = 15.9$ . For all the sets, the ranges of  $\langle n_x \rangle$  and  $\langle n_y \rangle$  were 13.0 to 16.7, and 14.4 to 18.5 respectively, which is almost symmetric about the values used for tuning. The set 75 data were reanalysed, with hits removed at random to reduce  $\langle n_x \rangle$  to 13.0 and  $\langle n_y \rangle$  to 16.7. The root-mean-square decreased by 7.9% in the  $x$ -module, and 3.7% in the  $y$ -module. If the larger of these is used, then a systematic uncertainty for the nominal sets due to sense plane aging is  $\pm 1.5 \times 10^{-4}$ .

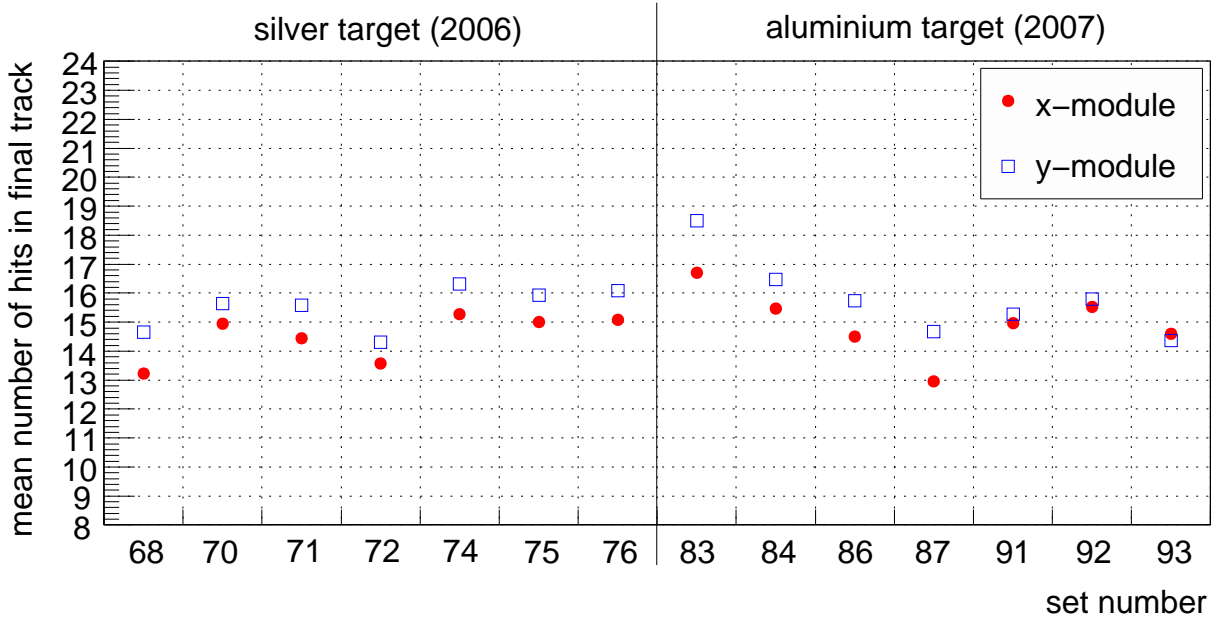


Figure 6.9: Mean number of hits in final TEC track, for each module. The  $c_x$  and  $c_y$  correction factors were tuned using set 75, which had  $\langle n_x \rangle = 15.0$  and  $\langle n_y \rangle = 15.9$ .

---

## 6.2.9 Summary of muon beam and fringe field uncertainties

First the discrepancies between beginning and end of set muon beam measurements were considered (Section 6.2.3). These are blamed on a problem with the reproducibility of the TECs' alignment, rather than a muon beam instability or a variation in the TEC drift cell response. The resulting alignment uncertainties are  $\pm 0.2$  cm for position and  $\pm 3$  mrad for angle. Second, the alignment of the magnetic field in position and angle was considered (Section 6.2.4), leading to uncertainties of  $\pm 0.1$  cm for position and  $\pm 1$  mrad for angle. These are combined in Section 6.2.5 using a Monte Carlo approach, and produce an uncertainty of  ${}_{-1.2}^{+6.4} \times 10^{-4}$  for  $\Delta P_{\mu}^{\pi} \xi$ .

The accuracy of the depolarisation through the magnetic field relies on the simulation's ability to reproduce large polarisation changes in three tests. The polarisation was lowered by either steering the muon beam away from the solenoid's symmetry axis (comparison I and II), or by inserting the TECs so that the muon beam's emittance was increased (comparison III); see Section 6.2.7 for a full description. A Monte Carlo approach was used to see how well the simulation reproduced the polarisation differences in the data. Using the original `Opera` field map, the largest discrepancy between data and simulation was  $2.0\sigma$ , which would not usually be a cause for concern. However, the `Opera` map is expected to differ from reality due to the quality of the initial conditions given, and the accuracy of the finite element method that is used to solve Maxwell's equations. Also the transverse field components ( $B_x$  and  $B_y$ ) from `Opera` could not be validated directly since they were not measured. Therefore although we believe that the original `Opera` map is close to the truth, we must assign an uncertainty that covers a potential error in the field map. This was evaluated by scaling the transverse magnetic field components, and observing where the agreement in the comparisons is minimised. The resulting uncertainty for  $\Delta P_{\mu}^{\pi} \xi$  is  ${}_{-0.0}^{+14.1} \times 10^{-4}$ .

Finally there are orthogonal systematic uncertainties from the degree to which the angle distributions of the muons could be reconstructed. There are contributions from the accuracy of multiple scattering in `GEANT3` ( $\pm 3.1 \times 10^{-4}$ ), from the algorithm used to reconstruct the muon trajectories ( $\pm 1.7 \times 10^{-4}$ ), and from the aging of the sense planes in the TECs ( $\pm 1.5 \times 10^{-4}$ ).

## 6.2.10 Stopping material

### Overview

About 80% of the muons stopped in a metal target, which also served as the shared cathode foil for the proportional chambers PC6 and PC7 (see Fig. 2.13). Events were accepted only if the muon produced a signal in PC6, but not in PC7. Muons that stopped in the PC6 gas (a mixture of  $\text{CF}_4$  and isobutane) or the wires were removed by cutting on the muon pulse width in PC5 and PC6 (see Section 3.3.3). This selected a sample of muons that mostly stopped in the metal foil. The relaxation was determined using a weighted asymmetry measurement (see Section 3.6). Each data set was fit with

$$P_\mu(t) = P_\mu^*(0) \exp(-\lambda t). \quad (6.3)$$

The relaxation rate from the data was used in the simulation.

There is one correction, one statistical uncertainty and four systematic uncertainties related to the stopping material. A correction to  $\Delta P_\mu^\pi \xi$  is necessary since the simulation used an incorrect  $\lambda$  value that was derived from an early analysis; re-generating the simulation would have required several months, so a correction must be made instead. A statistical uncertainty results from the precision with which  $\lambda$  can be determined from the data ( $\pm 2.4 \times 10^{-4}$ ). There is a systematic uncertainty from the degree to which stops in the PC6 chamber gas are eliminated ( $\pm 0.3 \times 10^{-4}$ ), and another uncertainty from muons that pass through the target and stop in PC7, but do not have enough energy to produce a signal ( $\pm 0.9 \times 10^{-4}$ ). A small fraction of muons are scattered from the target back into PC6, resulting in a systematic uncertainty of  $\pm 0.2 \times 10^{-4}$ . Lastly, there is an indication of a small bias in the asymmetry analysis, and this introduces a systematic uncertainty of ( $\pm 3.0 \times 10^{-4}$ ). After adding in quadrature the total systematic uncertainty is  $\pm 3.2 \times 10^{-4}$ . Note that for this analysis there is no uncertainty due to the choice of model for  $P_\mu(t)$  in the metals; see Section 1.6.3 for the theoretical arguments that demonstrate a strong preference for a single exponential form.

### Correction and statistical uncertainty

The results of the asymmetry analysis applied to the data are shown in Table 6.6, where the fit is made over the nominal time range of  $(1.05 < t < 9.00) \mu\text{s}$ . A weighted average

---

of these relaxation rates finds

$$\lambda_{\text{Ag}}^{\text{data}} = (0.813 \pm 0.079) \text{ ms}^{-1}, \quad (6.4)$$

$$\lambda_{\text{Al}}^{\text{data}} = (1.279 \pm 0.086) \text{ ms}^{-1}. \quad (6.5)$$

Note that these are consistent with the  $\mu^+$ SR results from Appendix H.8:

$$\lambda_{\text{Ag}}^{\mu\text{SR}} = (0.9 \pm 0.2 \text{ (stat.)} \pm 0.2 \text{ (syst.)}) \text{ ms}^{-1}, \quad (6.6)$$

$$\lambda_{\text{Al}}^{\mu\text{SR}} = (1.3 \pm 0.2 \text{ (stat.)} \pm 0.3 \text{ (syst.)}) \text{ ms}^{-1}. \quad (6.7)$$

The simulation used incorrect values of  $\lambda_{\text{Ag}} = 0.725 \text{ ms}^{-1}$  and  $\lambda_{\text{Al}} = 1.169 \text{ ms}^{-1}$ , and as a result the quantity  $\Delta P_{\mu}^{\pi} \xi$  must be corrected. The effect on the spectrum of a change in  $\lambda$  is calculated using

$$\frac{\int_{t_1}^{t_2} N(t) \cdot P_{\mu}^*(0) \exp(-\lambda_2 t) dt}{\int_{t_1}^{t_2} N(t) dt} - \frac{\int_{t_1}^{t_2} N(t) \cdot P_{\mu}^*(0) \exp(-\lambda_1 t) dt}{\int_{t_1}^{t_2} N(t) dt}, \quad (6.8)$$

where  $N(t) = N(0) \exp(-t/\tau_{\mu})$ ,  $\tau_{\mu}$  is the muon lifetime, and  $\lambda_1$  and  $\lambda_2$  are the relaxation rates between which the correction is being made. The time range is the same as the normal analysis ( $1.05 \mu\text{s} < t < 9.00 \mu\text{s}$ ). The common  $P_{\mu}^*(0)$  factor is close to 1.0, and its choice has a negligible impact on the correction. The quantity  $\Delta P_{\mu}^{\pi} \xi$  (the difference between the data and a hidden simulation value) is then corrected by  $+2.7 \times 10^{-4}$  for Ag ( $\lambda_1 = 0.725 \text{ ms}^{-1}$ ,  $\lambda_2 = 0.813 \text{ ms}^{-1}$ ) and  $+3.3 \times 10^{-4}$  for Al ( $\lambda_1 = 1.169 \text{ ms}^{-1}$ ,  $\lambda_2 = 1.279 \text{ ms}^{-1}$ ). The statistical uncertainty in determining  $\lambda$  from the data causes a  $P_{\mu}$  uncertainty of  $\pm 2.4 \times 10^{-4}$  for both targets, again using Eq. (6.8).

Table 6.6: Relaxation rate  $\lambda$  for each data set. The model  $P_\mu(t) = P_\mu^*(0) \exp(-\lambda t)$  has been fit over the nominal time range of  $(1.05 < t < 9.00) \mu\text{s}$ .

Set num.	Target	Description	$\lambda$ ( $\text{ms}^{-1}$ )	Fit quality	
				$\chi^2/\text{ndof}$	confidence
68	Ag	Stopping distrib. peaked $\frac{1}{3}$ into target	$0.71 \pm 0.24$	1.03	0.43
70	Ag	B = 1.96 T	$0.89 \pm 0.19$	0.62	0.90
71	Ag	B = 2.04 T	$0.93 \pm 0.20$	1.58	0.05
72	Ag	TECs-in, nominal beam	$0.85 \pm 0.19$	1.03	0.42
74	Ag	Nominal A	$1.02 \pm 0.24$	0.63	0.90
75	Ag	Nominal B	$0.85 \pm 0.19$	0.72	0.81
76	Ag	Steered beam A	$0.38 \pm 0.22$	0.52	0.96
	Ag	<b>Weighted average:</b>	<b><math>0.813 \pm 0.079</math></b>		
83	Al	Downstream beam package in place	$1.46 \pm 0.19$	1.85	0.01
84	Al	Nominal C	$1.10 \pm 0.21$	1.08	0.36
86	Al	Steered beam B	$1.21 \pm 0.18$	1.08	0.36
87	Al	Nominal D	$1.22 \pm 0.20$	0.85	0.65
91	Al	Lower momentum I	$1.63 \pm 0.40$	1.06	0.39
92	Al	Lower momentum II	$1.35 \pm 0.35$	0.98	0.49
93	Al	Lower momentum III	$1.32 \pm 0.27$	0.75	0.78
	Al	<b>Weighted average:</b>	<b><math>1.279 \pm 0.086</math></b>		

---

## Muon stops in gas

The distribution of the pulse widths in the PCs immediately before the target was described in Section 3.3.3. It is shown here in Fig. 6.10. The majority of the distribution is made up of stops in the metal target, which primarily contribute to zones 1 and 2, and there is a “gas band” that runs approximately parallel to the cut-B line and contributes mostly to zones 2 and 3. The analysis selects only zone 1; the cut-B line removes almost all of the gas contamination, but a small fraction still makes it to zone 1.

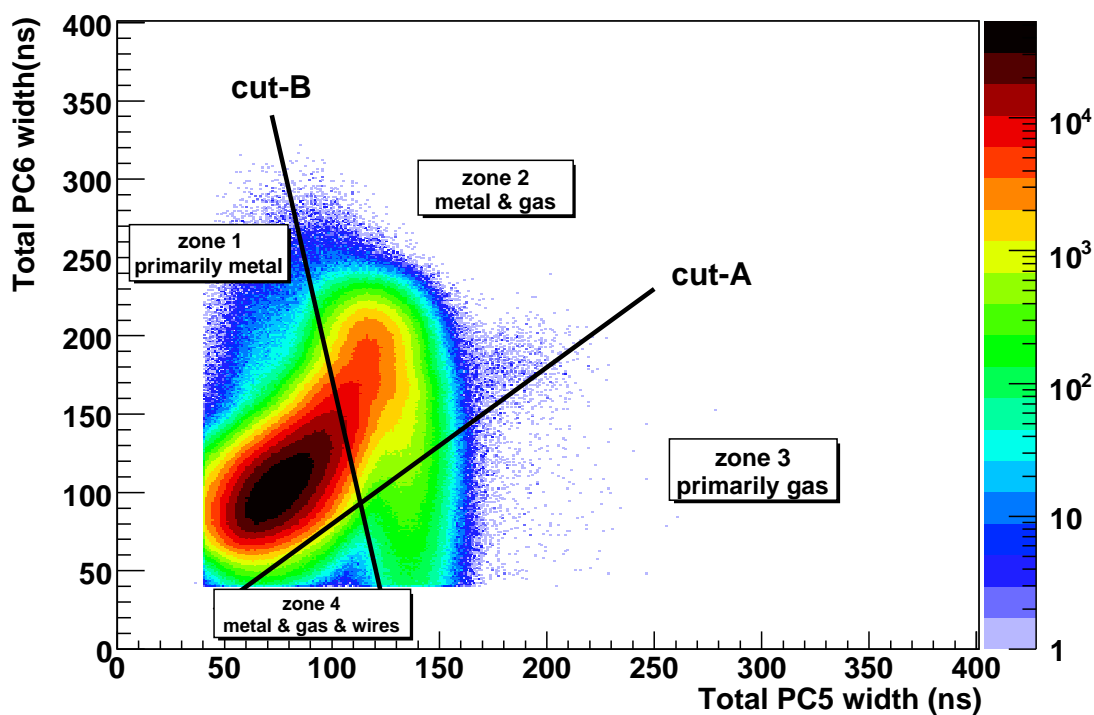


Figure 6.10: Muon pulse widths in PC5 and PC6 (the proportional chambers immediately before the metal stopping target). For data, the stops in gas appear as a band that is approximately parallel to cut-B, primarily contributing to zones 2 and 3.

A systematic uncertainty was estimated using only the data. This required three numbers that are described in Appendix J: the depolarisation in gas (8.0%), the fraction of the total PC6+target stops in gas ( $f_g$ ), which is between 4% and 7% depending on the set, and the fraction of the gas distribution in zone 2 that leaks into zone 1 (tuned to be  $< 0.5\%$  by adjusting cut-B). If the number of muons stopping in the gas in zone  $i$  is

denoted  $N_i^g$ , then

$$f_g N_{\text{total}} = N_1^g + N_2^g + N_3^g + N_4^g, \quad (6.9)$$

$$N_1^g < 0.5\% \times (N_1^g + N_2^g), \quad (6.10)$$

which gives

$$\frac{N_1^g}{N_{\text{total}}} < 0.5\% \times \left[ f_g - \frac{N_3^g + N_4^g}{N_{\text{total}}} \right]. \quad (6.11)$$

If all the gas stops are conservatively assumed to be in zones 1 and 2 so that  $N_3^g = N_4^g = 0$ , and  $f_g$  is set to its maximum value of 7%, then an upper limit on the systematic uncertainty from muons stopping in PC6 gas is  $8.0\% \times 0.5\% \times 7\% = 0.3 \times 10^{-4}$ .

A special simulation found that no more than 0.11% of muons entered PC7 (the wire chamber *after* the metal stopping target), but did not have enough energy to produce a signal. These stop in the PC gas, and experience a depolarisation of 8.0% (see above). An upper limit for the systematic uncertainty due to these stops is therefore  $0.11\% \times 8.0\% = 0.9 \times 10^{-4}$ . The same simulation determined that 0.02% of muons enter the target volume, but are scattered back into PC6, and pass all the analysis cuts. These contribute a negligible systematic uncertainty of  $0.02\% \times 8.0\% = 0.2 \times 10^{-4}$ .

### Analysis bias

The asymmetry analysis is applied to the simulation to confirm that the input values of  $\lambda$  can be recovered ( $\lambda_{\text{Ag}}^{\text{input}} = 0.725 \text{ ms}^{-1}$  and  $\lambda_{\text{Al}}^{\text{input}} = 1.169 \text{ ms}^{-1}$ ). The results of this study are shown in Fig. 6.11, where the simulation that accompanies set 74 (nominal) is seen to have a  $\lambda$  value that is 3.4 standard deviations below the input value. As a result, the *weighted average* of  $\lambda$  for the silver simulations is 2.4 standard deviations from the input; the weighted average for the aluminium simulations is consistent with the input  $\lambda$ .

An exhaustive investigation attempted to find the cause of the discrepancies for the silver simulations. The results were found to be robust to the binning, weighting strategy and time range used in the asymmetry analysis. The confidence levels from the asymmetry analysis were spread evenly between 0 and 1, indicating that the  $\lambda$  uncertainties are properly determined. A separate analysis that made fits to the upstream and downstream time distributions (*i.e.* an asymmetry was not constructed) confirmed the  $\lambda$  results, but with inferior statistical precision. The simulation for set 74 only differed from the other nominal sets in its input beam profile and muon/positron rates; the beam profile produced a reasonable value for  $P_\mu(0)$ , and the rate differences from the other sets were insignificant.

---

We note that an additional statistically independent simulation of set 74 (not used here in the weighted averages) produced  $\lambda = (0.59 \pm 0.17) \text{ ms}^{-1}$ , which is consistent with both the input value ( $\lambda = 0.725 \text{ ms}^{-1}$ ) and the anomalous result from the earlier set74 simulation ( $\lambda = (0.32 \pm 0.12) \text{ ms}^{-1}$ ); clearly significant additional statistics are needed to make a firm conclusion. Since the investigation could not find a reason to reject the anomalous  $\lambda$  result, we are forced to admit the possibility that a systematic  $\lambda$  uncertainty exists due to an analysis bias, or the  $\lambda$  statistical uncertainties from the asymmetry analysis are underestimates.

We are not aware of a credible mechanism that would create a different bias for the silver and aluminium targets. Therefore the average discrepancy between the input and measured  $\lambda$  from the simulation ( $0.5 \times (2.4 + 0.0)\sigma = 1.2\sigma$ ) is taken as an additional uncertainty that must be applied to the *data*. Using Eqs. (6.4), (6.5) and (6.8), this results in a systematic uncertainty of  $\pm 2.9 \times 10^{-4}$  for silver and  $\pm 3.1 \times 10^{-4}$  for aluminium. The average of these ( $\pm 3.0 \times 10^{-4}$ ) is applied to all sets as the systematic uncertainty due to a potential analysis bias.

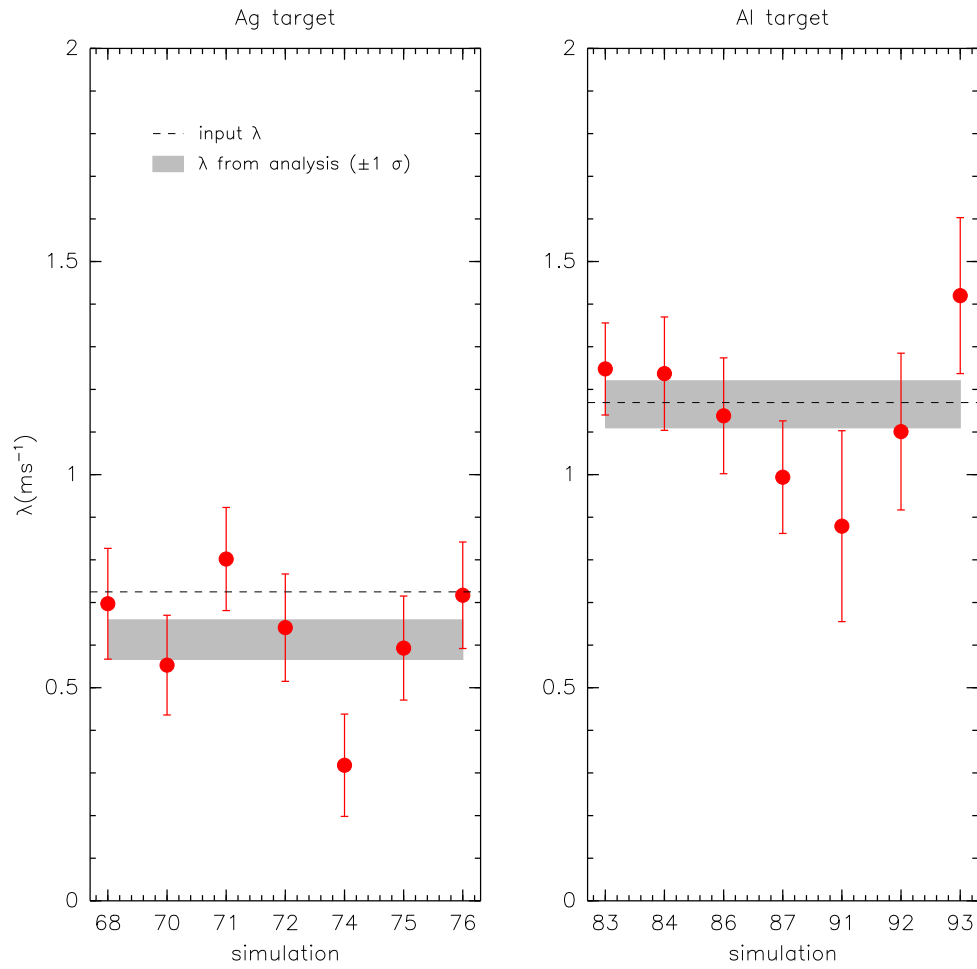


Figure 6.11: The result of the asymmetry analysis applied to the simulations[103]. The relaxation rate ( $\lambda$ ) for the set 74 simulation is  $3.4\sigma$  away from the input value.

---

### 6.2.11 Muon production target

The simulation generates muons with anti-parallel spin and momentum vectors, starting from the position of the TECs. This neglects multiple scattering in the muon production target and the beam line vacuum window, which changes the momentum vector but not the spin. This is treated here as a systematic correction with an associated uncertainty. (The difference in precession frequencies of the momentum and spin through the M13 beam line is neglected since it introduces an error of  $< 10^{-8}$ ; see Appendix I).

Surface muons are produced with  $p \approx 29.79$  MeV/c, but the beam line was nominally tuned to accept muons with an average momentum of  $\langle p \rangle = 29.6$  MeV/c. Therefore the muons lost 0.19 MeV/c of momentum on average, which is equivalent to  $\approx 3.8$  mg/cm<sup>2</sup> in graphite. (The 3  $\mu$ m beam line vacuum window can be safely neglected since it corresponds to just 0.3 mg/cm<sup>2</sup> of material.) The width of the resulting multiple scattering distribution<sup>41</sup>,  $\theta_0$ , is found to be 9.3 mrad using a **GEANT4** simulation[103]. The uncertainty is conservatively estimated as  $\pm 17\%$  based on the observed discrepancy for **GEANT3** from Section 6.2.8. The degree to which the spin is depolarised with respect to the momentum is then estimated by  $\cos(\theta_{\text{space}}^{\text{rms}})$ , where  $\theta_{\text{space}}^{\text{rms}} = \sqrt{2}\theta_0$ . This results in a correction to the simulation's  $P_\mu$  of  $(-0.9 \pm 0.3) \times 10^{-4}$ , which is a correction to  $\Delta P_\mu^\pi \xi$  of  $(+0.9 \pm 0.3) \times 10^{-4}$ .

The **GEANT4** simulations are repeated for the lower momentum sets. The widths are  $\theta_0 = 24.2$  mrad for  $\langle p \rangle = 28.75$  MeV/c, and  $\theta_0 = 22.9$  mrad for  $\langle p \rangle = 28.85$  MeV/c. These correspond to  $\Delta P_\mu^\pi \xi$  corrections of  $(5.9 \pm 1.9) \times 10^{-4}$  and  $(5.2 \pm 1.6) \times 10^{-4}$ , respectively. The uncertainty for this correction will be applied set-dependently in Chapter 7, although in practice this detail makes no difference to the final answer.

---

<sup>41</sup> $\theta_0$  is the standard deviation of a Gaussian fit to the central 98% of the plane-projected multiple scattering distribution.

### 6.2.12 Background muon contamination

The true muon stopping distribution is not available for the data, and we can only measure the last plane that registered a muon hit. In the previous  $P_\mu^\pi \xi$  analysis this distribution did not agree well in data and simulation unless an additional source of pion decays was included in the upstream beam package area (see Fig. 6.12(a)). An upper limit on the effect of these “background muons” was calculated as  $1.8 \times 10^{-4}$ , assuming they have opposite polarisation to the surface muons. For the current analysis the agreement is better *without* the additional pion source; this is demonstrated in Fig. 6.12(b), where improvements in the classification have increased the number of downstream events in the simulation relative to the data. If anything, the simulation now has *more* downstream muons for planes 35 onwards<sup>42</sup>, and even this excess is at the level of  $< 10^{-5}$ . Therefore the background muon contamination is now reduced to a negligible level, and this part of the systematic uncertainty is zero.

However, the data-simulation discrepancies in planes 35 to 53 (and in planes 10 to 20) do introduce a systematic uncertainty; the simulation’s stopping distribution must match the data, since high angle muons that undergo more depolarisation are preferentially stopped further upstream. Figure 6.12(b) indicates that the mean stopping position and/or its shape are not reproduced by the simulation. The most accurate measurement of the mean muon stopping distribution comes from the energy calibration procedure (see Section 3.5). The reconstructed spectrum endpoint depends on the thickness of target (and detector) material traversed, which results in a dependence on  $1/\cos\theta$ . The gradient of this relationship,  $\alpha_{\text{up}}$  or  $\alpha_{\text{down}}$  for upstream and downstream respectively, is therefore a measure of the material traversed by the upstream and downstream decay positrons. The stopping distribution can then be measured using

$$\alpha_{\text{diff.}} = \alpha_{\text{up}} - \alpha_{\text{down}}. \quad (6.12)$$

The energy calibration procedure finds the difference in reconstructed spectrum endpoint between data and simulation, which has a gradient equal to

$$\alpha_{\text{up}}^{\text{data}} - \alpha_{\text{up}}^{\text{sim.}}, \quad (6.13)$$

---

<sup>42</sup>Planes 53 to 56 in Fig. 6.12(b) suggest there are more muons in the data than the simulation. However, these are beam positrons that are mistakenly identified as muons in the data due to an imperfect separation of pulse width in the proportional chambers. This does not occur in the simulation, where the separation between muons and beam positrons is perfect.

---

in the upstream half of the detector, and

$$\alpha_{\text{down}}^{\text{data}} - \alpha_{\text{down}}^{\text{sim.}} \quad (6.14)$$

in the downstream half. The difference between the gradients in the upstream and downstream half (*i.e.* Eq. (6.13) minus Eq. (6.14)) is then

$$\left(\alpha_{\text{up}}^{\text{data}} - \alpha_{\text{down}}^{\text{data}}\right) - \left(\alpha_{\text{up}}^{\text{sim.}} - \alpha_{\text{down}}^{\text{sim.}}\right) = \alpha_{\text{diff.}}^{\text{data}} - \alpha_{\text{diff.}}^{\text{sim.}}, \quad (6.15)$$

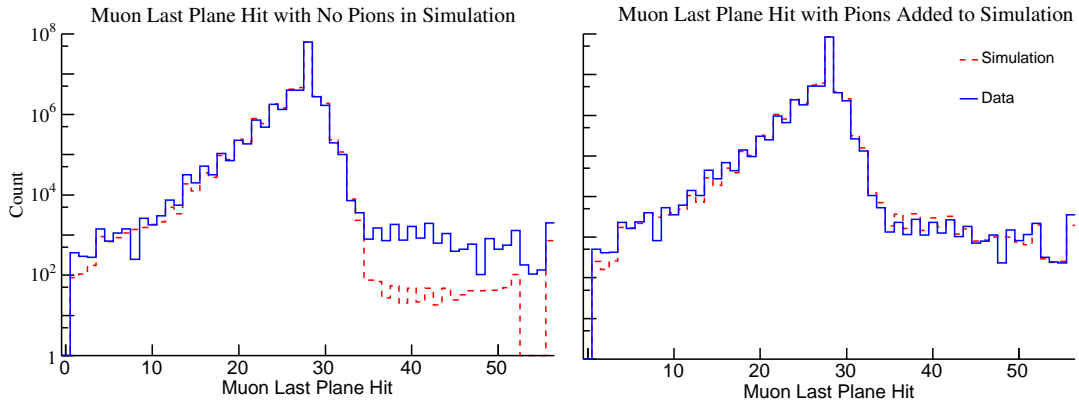
which measures how well the muon stopping distributions agree in data and simulation.

The stopping distribution measure from Eq. (6.15) is shown in Fig. 6.13. For five of the simulations, the mean of the muon last plane distribution was matched by adding an extra 1.9 mg/cm<sup>2</sup> of material to the simulation (see Section 2.11), and the resulting disagreement is  $(5.5 \pm 1.4)$  keV/c on average. For the other simulations no additional material was added, and this improved the data-simulation disagreement to  $(0.2 \pm 1.1)$  keV/c (We note that although  $\alpha_{\text{diff.}}^{\text{data}} - \alpha_{\text{diff.}}^{\text{sim.}}$  is an accurate measurement of the stopping distribution, it is clearly not precise. For this reason it could not be used to tune the simulation so that it matched the data.)

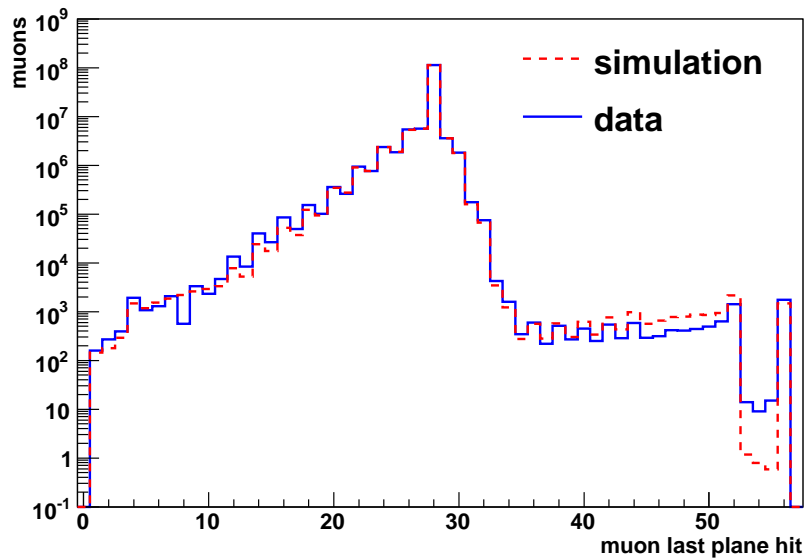
The simulation can determine the relationship between  $P_{\mu}(0)$  and  $(\alpha_{\text{diff.}}^{\text{data}} - \alpha_{\text{diff.}}^{\text{sim.}})$ . This depends on the beam profile, and is within the range  $(0.04 - 0.25) \times 10^{-4}/(\text{keV}/c)$ , with an average of  $0.13 \times 10^{-4}/(\text{keV}/c)$ . The systematic uncertainty from matching the stopping distribution is therefore  $\pm 5.5 \times 0.13 \times 10^{-4} = \pm 0.7 \times 10^{-4}$  for the sets with the extra 1.9 mg/cm<sup>2</sup> of material. This result is an approximation since it averages over the silver and aluminium targets, where differences are expected in the data-simulation agreement. Since this is a small number and only applies to 5 of the 14 simulations, it is treated as a conservative systematic uncertainty rather than a correction. An additional piece of the same magnitude is added in quadrature to account for a small difference in stopping distribution shape, resulting in a total systematic uncertainty of  $\pm 1.0 \times 10^{-4}$ .

*The remaining systematic uncertainties are related to the decay positron reconstruction. They are mostly evaluated by exaggerating a setting in the simulation or analysis. The exaggerated spectrum is then fit to the original spectrum in order to determine the change in the muon decay parameters (MPs). The exaggeration factors are made as large as possible to obtain statistically meaningful MP changes, while maintaining a linear relationship with the MPs. The changes in MPs are then scaled down according to how large the effect could actually be, resulting in the systematic uncertainty. When the original*

and exaggerated spectra are highly correlated (i.e. they contain a large number of events with identical energy and angle), the spectrum fit will have a reduced  $\chi^2$  that is much smaller than one, and the uncertainty in the  $P_{\mu}^{\pi} \xi$  change will therefore be too large. In this case the uncertainties in the MPs are scaled down so that the reduced  $\chi^2$  is equal to one, corresponding to multiplication by  $\sqrt{\chi^2/\text{ndof}}$ .



(a) Distribution of last plane that measures the muon, for data and simulation, from the previous analysis (originally Fig. 6.9 from Ref. [57]). The mismatch is resolved by including an additional source of pion decays at the location of the upstream beam package.



(b) The same figure re-made for the current analysis, where *no* additional pion decays are added.

Figure 6.12: Background muon contamination in the two  $P_{\mu}^{\pi} \xi$  analyses.

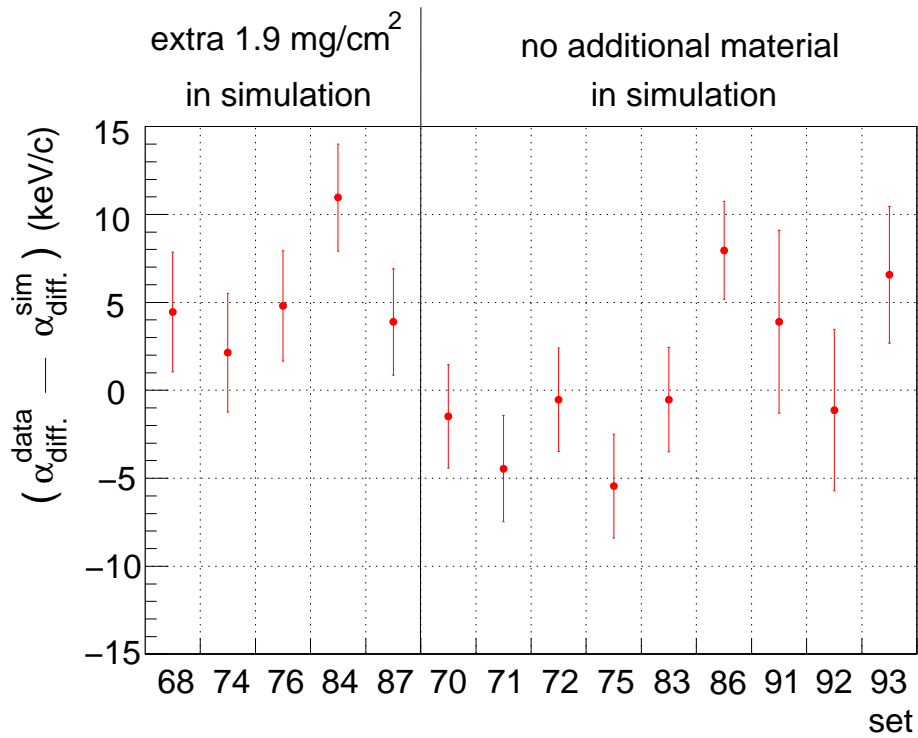


Figure 6.13: The muon stopping distribution is most accurately measured in data and simulation using the endpoint calibration; see the main text for a description of the ordinate. The data and simulation distributions are in agreement when  $\alpha_{\text{diff.}}^{\text{data}} - \alpha_{\text{diff.}}^{\text{sim.}} = 0$ .

---

## 6.3 Chamber response

### 6.3.1 Drift chamber space-time relationship

The space-time-relationships (STRs) in the drift cells were optimised by minimising the residual between the hit times from the drift cell, and the times that best fit the helix trajectories (see Section 3.2.7). In the simulation, where it was sufficient to use a single STR cell for all wires and planes, this procedure effectively absorbs a small bias from the helix fitting into the STRs. In data, where a separate STR cell was obtained for each plane<sup>43</sup>, the procedure corrects for plane-to-plane construction and response differences, in addition to any small bias from the helix fitting algorithm.

The refinement procedure was carried out iteratively, with the STR forced to remain smooth at each step. After convergence, there were residuals in the drift cell corresponding to regions where manipulating the STRs could not bring the drift time closer to the fitted trajectory. The amount by which these residuals differ in data and simulation is the basis of the chamber response systematic uncertainty.

The difference between the data and simulation residuals at the final iteration is shown in Fig. 6.14. The data results are averaged over all planes. Only half a cell is shown, and in practice this is reflected about the line  $uv = 0$ . The largest discrepancies between data and simulation are at the edge of the cell ( $u$  or  $v = 0.2$  cm), where there were low statistics and the single hit resolution was degraded. In the rest of the cell the variations are at the impressive level of  $< 4$  ns.

The following approach exaggerated the differences between data and simulation without breaking the smoothness of the STRs:

1. Generate a separate refined STR cell for each plane in the simulation.
2. For each plane, find the difference in residuals at the final iteration, just like Fig. 6.14. Fit this distribution with a fifth order polynomial function.
3. Exaggerate the polynomial function until the  $\chi^2/\text{ndof}$  of positron helix fits becomes a factor of two worse. This corresponds to the single hit resolution being degraded by  $\approx (\sqrt{2} - 1) \approx 40\%$ , and requires the polynomial function to be exaggerated by a factor of ten.

---

<sup>43</sup>One STR cell was used for the whole plane. The cell is therefore an average over all the cells within the plane.

4. Re-analyse the simulation with the scaled STRs, and compare to the nominal simulation.

5. Reduce the change in  $P_\mu^\pi \xi$  by the scale factor of ten.

The change in  $P_\mu^\pi \xi$  from this procedure is  $2.0 \times 10^{-4}$ . However, the exaggeration of errors in the STRs also worsens the reconstruction resolution, for which there is already an orthogonal systematic uncertainty. In order to avoid double-counting with the resolution systematic uncertainty, a subtraction of  $1.1 \times 10^{-4}$  is necessary, leading to a final systematic uncertainty from the STRs of  $\pm 0.9 \times 10^{-4}$ .

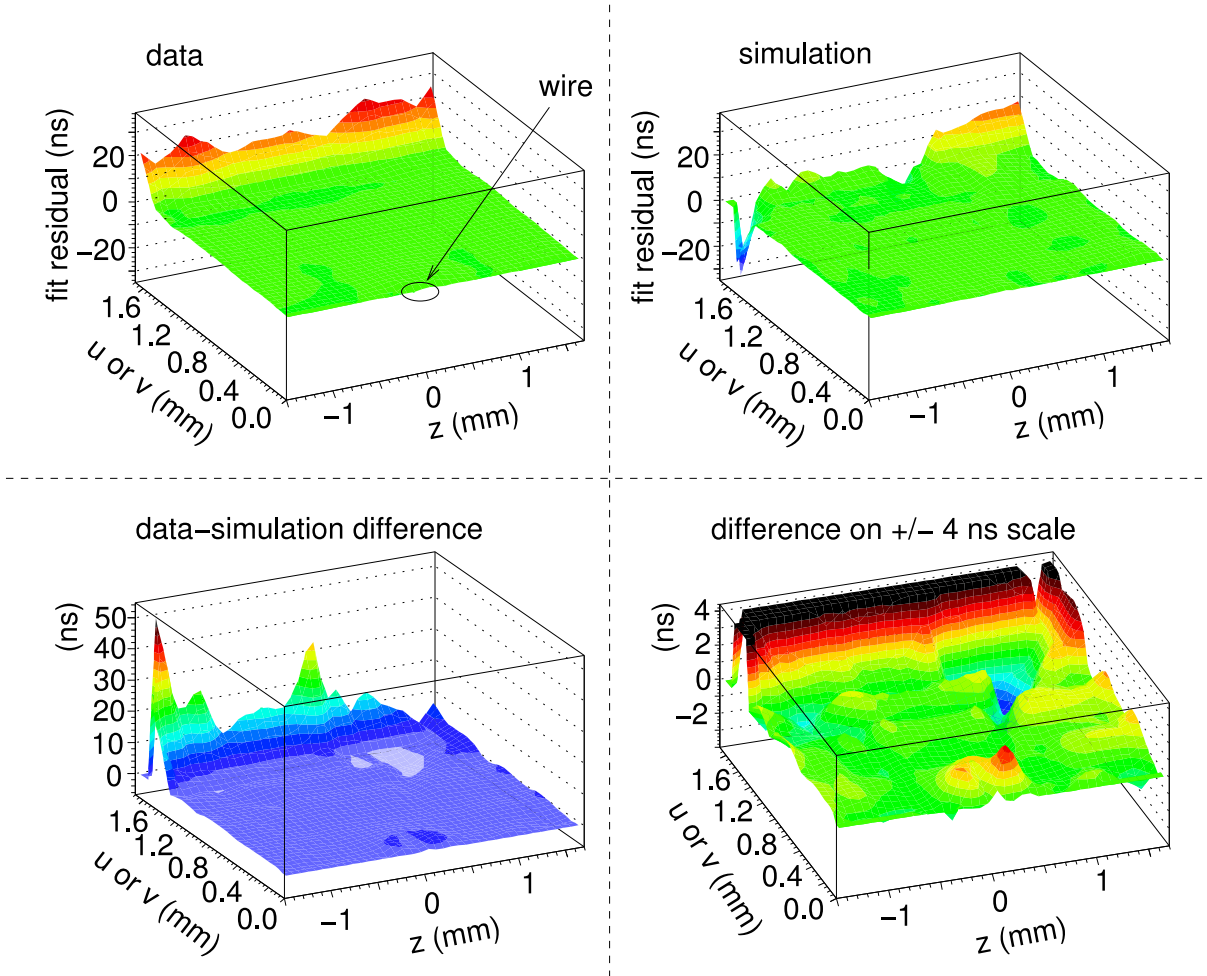


Figure 6.14: An example of the time residuals from the helix fit, after refining the space-time-relationships. Only half a cell is shown, which in practice is reflected about  $uv = 0$ .

---

### 6.3.2 Drift chamber geometric effects

In the simulation, the drift chamber foils are always at the same, well-known positions. In the real chambers there are three uncertainties in the shape and position of the foils: i) the absolute foil positions are only known to better than  $100\ \mu\text{m}$ , ii) the foils have an absolute bulge (inwards or outwards) of up to  $60\ \mu\text{m}$ , and iii) the bulge in the foils varies by up to  $35\ \mu\text{m}$  during data acquisition. A change in the foil position can reduce or increase the number of hits that are available for the helix fitting algorithm, and this introduces a systematic uncertainty.

An upper limit on the systematic uncertainty uses a simulation with the chamber foils moved inwards<sup>44</sup> by  $500\ \mu\text{m}$ . This changes  $\Delta P_\mu^\pi \xi$  by  $(6.7 \pm 5.4) \times 10^{-4}$ . Using the largest foil position uncertainty of  $100\ \mu\text{m}$ , this corresponds to a systematic uncertainty of  $(100/500) \times 6.7 \times 10^{-4} = \pm 1.3 \times 10^{-4}$ .

### 6.3.3 Upstream-downstream efficiency

The simulation must reproduce the difference in track reconstruction efficiency (TRE) between the upstream and downstream halves of the detector. This is measured in data and simulation using a special “upstream stops” analysis, where muons are stopped close to the trigger scintillator, and the decay positrons are reconstructed independently in each half of the detector. The TRE is then calculated based on how often a positron is reconstructed in one half of the detector, but not in the other.

The difference in TRE between data and simulation is shown in Fig. 6.15, where a cut has been placed at  $(23 < p < 29)\ \text{MeV}/c$  to remove the area of phase space that is contaminated with a beam positron background. There is evidence that the TRE depends on  $|\cos\theta|$ , but not on  $p$ . The systematic uncertainty is evaluated by multiplying the number of upstream counts by i) a constant to measure the  $p$ -contribution, and ii) a linear function to measure the  $|\cos\theta|$ -contribution. After averaging over the aluminium and silver targets, the  $p$ -contribution is  $1.3 \times 10^{-4}$ , and the  $|\cos\theta|$ -contribution is  $0.2 \times 10^{-4}$ . These are added in quadrature to give a total efficiency systematic uncertainty of  $\pm 1.4 \times 10^{-4}$ .

---

<sup>44</sup>The systematic uncertainty is symmetric since the real cells can be thicker or thinner than their nominal positions. The systematic uncertainty is evaluated using simulation, where it is only straightforward to move the foils inward.

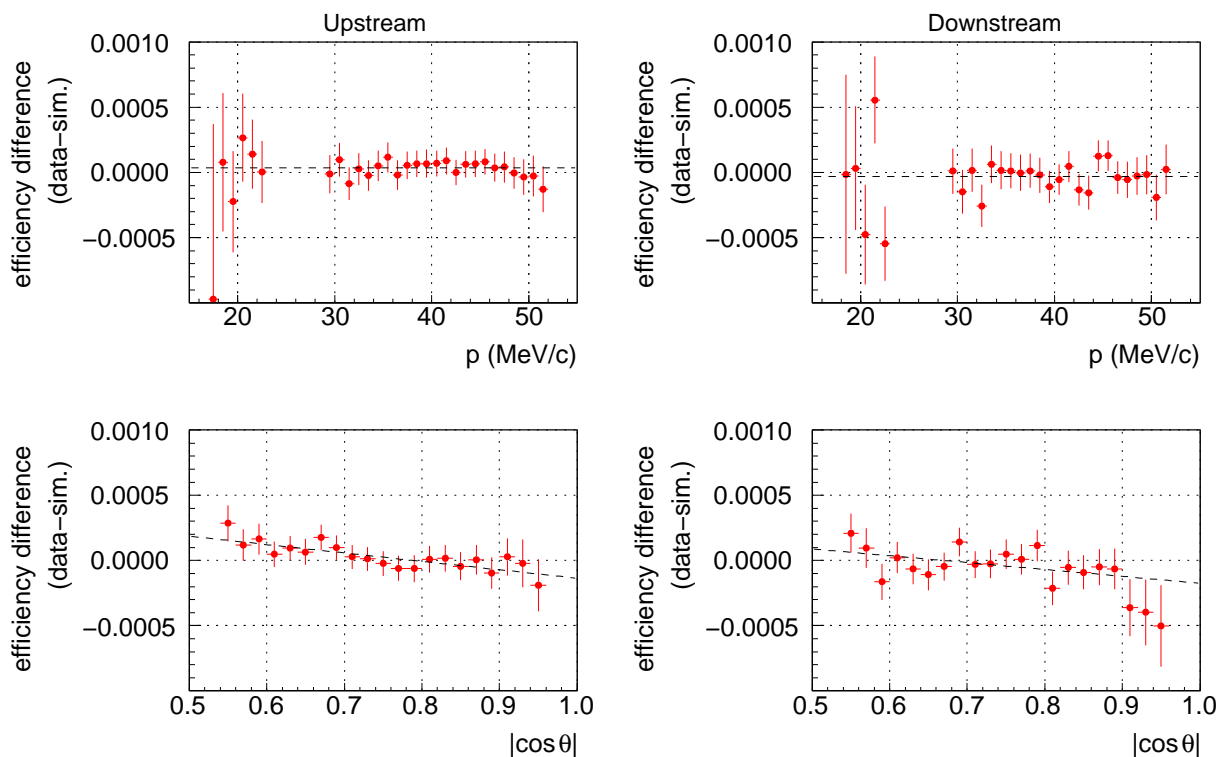


Figure 6.15: Track reconstruction efficiency for the kinematic fiducial. The results for the aluminium target are shown. The upstream efficiency is determined by how often a positron is reconstructed in the downstream half of the detector, but not in the upstream half. The definition is reversed for the downstream efficiency. A cut has been placed at  $(23 < p < 29)$  MeV/c in order to remove beam positrons. The dashed lines are simple linear fits that are used to characterise the dependence on angle.

### 6.3.4 Crosstalk

The origin and removal of electronic crosstalk is described in Section 3.2.2. A limit was set on a systematic uncertainty from crosstalk by re-analysing a data set with the crosstalk removal routine disabled. The change in  $\Delta P_\mu^\pi \xi$  was  $0.5 \times 10^{-4}$ , and this is used here as the systematic uncertainty (the scale factor is effectively one).

### 6.3.5 Wire time offsets

In the previous  $P_\mu^\pi \xi$  analysis the wire time offsets were only calibrated at the beginning and end of the run period. The calibration data were acquired with the magnetic field off, using 120 MeV/c pions and a special downstream trigger. There were significant differences between the two calibrations, and the  $P_\mu^\pi \xi$  result changed by  $9 \times 10^{-4}$  depending

---

on which calibration was used[57].

For this measurement a reliable downstream trigger was in place throughout the acquisition of data. The wire time offsets in each half of the detector were calibrated on a set-by-set basis using the decay positrons (see Section 3.2.1). Beam positrons that passed through the entire detector were then used to determine the relative timing of the upstream and downstream halves of the detector.

There are two systematic uncertainties from this procedure: a bias from the calibration technique, and the degree to which the relative upstream/downstream timing could be established. The systematic uncertainty due to a bias was evaluated as  $\pm 0.04 \times 10^{-4}$ , and will therefore not be discussed here (see Ref. [79] for further details). The relative timing of the upstream and downstream halves was determined to better than 0.10 ns. An exaggerated upstream-downstream shift of 10 ns changes  $\Delta P_\mu^\pi \xi$  by  $(82 \pm 7) \times 10^{-4}$ . After scaling down by  $10 \text{ ns}/0.10 \text{ ns} = 100$ , this results in a systematic uncertainty of  $\pm 0.8 \times 10^{-4}$ .

### 6.3.6 Negligible chamber response uncertainties

An additional three chamber response systematic uncertainties were considered, but were not large enough to require recognition in Table 6.1, although they were included in the previous  $P_\mu^\pi \xi$  analysis.

When a decay positron crossed the same drift cell as the muon, there was reduced gain for the positron due to lingering muon ionisation (the chamber had a “dead zone”). The simulation included this dead zone by removing hits within 0.06 cm of the muon hit along the wire, during a recovery time of  $3.0 \mu\text{s}$ . These parameters were tuned according to the fraction of hits removed by the dead zone in data. In the simulation this corresponded to 0.03% of hits, tuned to an accuracy of about 20% (*i.e.*  $\pm 0.006\%$  of the total number of hits) A special simulation was run with an enhanced dead zone: instead of only removing positron hits within 0.06 cm of the muon hit, the entire wire was made insensitive to decay positrons for the  $3.0 \mu\text{s}$  recovery time. Inclusion of the enhanced dead zone changes  $\Delta P_\mu^\pi \xi$  by  $(25 \pm 2) \times 10^{-4}$ , and removes 0.99% of hits. Compared to the nominal case, this special simulation exaggerates the removed hits by  $0.99\% - 0.03\% = 0.96\%$ , resulting in a scale factor of  $0.96\%/0.006\% = 160$ . The change in  $\Delta P_\mu^\pi \xi$  is then  $(1/160) \times 25 \times 10^{-4}$ , which is a systematic uncertainty of just  $\pm 0.2 \times 10^{-4}$ .

For the previous  $P_\mu^\pi \xi$  analysis, the wires in the simulation were placed at exactly the centre of the cathode foils. In reality, they were determined to be offset from the centre

by  $150\ \mu\text{m}$ , and this introduced a systematic uncertainty of  $\pm 2.2 \times 10^{-4}$ . The current analysis includes the offset in the simulation, eliminating this uncertainty altogether.

In the simulation the gas density inside the drift chambers is constant, but for the data it tracks the atmospheric pressure and the exterior temperature, which results in drift cell space-time-relationships (STRs) that vary over a data set. The previous analysis used the same STRs for all the data, and a systematic uncertainty of  $(0.2 \pm 0.2) \times 10^{-4}$  was established based on the RMS variation in density[83], and  $(1.7 \pm 1.0) \times 10^{-4}$  based on the largest variation in density[57]. For the current analysis, each run was analysed with STRs that were corrected for the atmospheric pressure and temperature, meaning the systematic uncertainty is much smaller than  $\pm 0.2 \times 10^{-4}$ . Therefore the change in STRs due to gas density is a negligible effect, and is no longer evaluated.

## 6.4 Detector alignment

Two systematic misalignments of the drift chambers have been previously considered[83]: a “shear”, where each detector plane is offset in  $u$  or  $v$  from the previous one by a constant amount, and a “corkscrew”, where each detector plane is rotated about the  $z$ -axis from the previous one by a constant angle. Stringent limitations from the detector design meant these systematic uncertainties had negligible values of  $\pm 0.009 \times 10^{-4}$  and  $\pm 0.020 \times 10^{-4}$  for the shear and corkscrew, respectively. These were not re-evaluated for the current measurement, and are simply discarded. Random misalignments are not considered, since these smear the tracking residuals and degrade the resolution, which is handled as an orthogonal systematic uncertainty (see Section 6.6).

The length ( $z$ ) and width ( $u, v$ ) scales are used to determine the momentum components of the reconstructed helices. The systematic uncertainties from these scales are re-evaluated for the current measurement. The  $z$  length scale is known to  $50\ \mu\text{m}$  out of  $100\ \text{cm}$ , which is a fractional uncertainty of  $5.0 \times 10^{-5}$ . A special analysis made a fractional change of  $1 \times 10^{-3}$  to the  $z$ -component of the momentum, which is a factor of 20 larger than the true uncertainty. The change in  $P_\mu^\pi \xi$  is  $(0.5 \pm 5.2) \times 10^{-4}$ , which leads to a systematic uncertainty of  $(1/20) \times 0.5 \times 10^{-4} = \pm 0.03 \times 10^{-4}$ .

For the width scale, the wires were positioned in a plane to better than  $5\ \mu\text{m}$ ; a wire plane is  $32\ \text{cm}$  in width, corresponding to a fractional uncertainty of  $2 \times 10^{-5}$ . The sensitivity of  $P_\mu^\pi \xi$  was determined in a similar way to the length scale: a special analysis made a fractional change of  $1 \times 10^{-3}$  in both the  $u$ - and  $v$ -components of the momentum,

---

finding that  $P_\mu^\pi \xi$  changes by  $(7.8 \pm 5.2) \times 10^{-4}$ . This time the systematic uncertainty is scaled down to  $(2 \times 10^{-5}) / (1 \times 10^{-3}) \times 7.8 \times 10^{-4} = \pm 0.2 \times 10^{-4}$ .

## 6.5 Positron interactions

### 6.5.1 Bremsstrahlung and $\delta$ -electron rates

Uncertainties from the simulation’s continuous energy loss model are part of the energy calibration uncertainties in Section 6.7.2. In this section the uncertainties from discrete processes are described; the most important of these are  $\delta$ -electron production (where an electron is knocked out of an atomic orbital) and Bremsstrahlung (“braking radiation”, where one or more photons are radiated during deceleration, significantly changing the energy of the positron). The simulation must accurately reproduce these processes since the extra tracks interfere with the reconstruction. Specifically there are three effects: first, the number of chamber hits will differ in data and simulation; second, the  $\delta$ -electrons and Bremsstrahlung represent invisible energy loss contributions that cause the positron to be reconstructed with a different energy and angle than the original decay kinematics; third, the processes can “break” the track by introducing a large angle change, and this prevents reconstruction. Approximations in the GEANT3 physics and uncertainties in material thicknesses can also cause the simulation’s rates to differ from data.

The  $\delta$ -electron rate is compared in data and simulation by selecting events where the decay positron trajectory is broken in two, with an additional electron track originating from the point where the track is broken. The momentum of the electron track is well correlated with the momentum difference between the two broken track halves, indicating that genuine  $\delta$ -electrons are being measured (see Fig. 6.16). A special simulation with the production of  $\delta$ -electrons disabled confirmed that the background of the measurement is small.

The momentum distributions of the reconstructed electrons are compared for nominal data and simulation on the left of Fig. 6.17, where the reconstruction efficiency is seen to decrease below 6 MeV/c. Using the range  $(6 < p_\delta < 16)$  MeV/c and all the available data sets, the ratio of  $\delta$ -electrons in data and simulation is  $1.007 \pm 0.009$  (*i.e.* the central value indicates a deficit of  $\delta$ -electrons in the simulation, but this is not statistically supported).

A special simulation is used with the  $\delta$ -electron probability increased by a factor of three, changing  $P_\mu^\pi \xi$  by  $(25 \pm 7) \times 10^{-4}$ . For this simulation, the reconstructed  $\delta$ -electrons are compared for the nominal and special simulation on the right of Fig. 6.17, where the

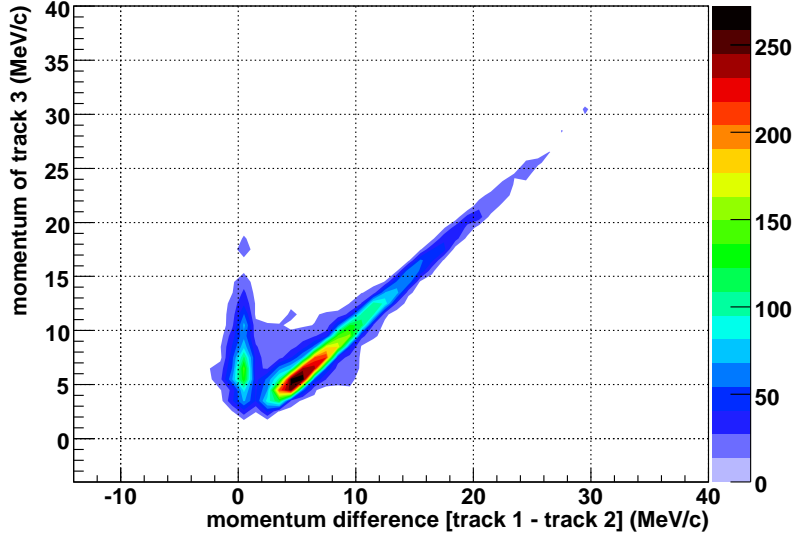


Figure 6.16: Validation of the  $\delta$ -electron measurement method. Events are selected with a decay positron track that is broken in half, becoming tracks 1 and 2, with an additional negative particle originating from the break point (track 3). The observed correlation indicates that  $\delta$ -electrons are being measured.

ratio of counts is  $2.80 \pm 0.04$ ; the ratio is not exactly 3.0 due to second order effects. The systematic uncertainty is then

$$\frac{1.007 - 1.0}{3.0 - 1.0} \times 25 \times 10^{-4} = \pm 0.1 \times 10^{-4}. \quad (6.16)$$

Note that using 2.80 instead of 3.0 in the denominator does not change the systematic uncertainty by a significant amount.

The Bremsstrahlung rate is compared in data and simulation using a similar approach to the  $\delta$ -electrons: events are selected with a “broken” decay positron trajectory, and the momentum difference between the two halves of the track is shown on the left side of Fig. 6.18. Another special simulation is used with the Bremsstrahlung probability increased by a factor of three, and this changed  $P_{\mu}^{\pi} \xi$  by  $(55 \pm 7) \times 10^{-4}$ ; the effect on the broken track momentum difference is shown on the right side of Fig. 6.18. Using the momentum range of  $(15 < p < 35)$  MeV/c, the ratio of Bremsstrahlung events in data and simulation averaged over all sets is  $1.024 \pm 0.004$ . The ratio between the nominal and increased

---

Bremsstrahlung rate simulations is  $2.82 \pm 0.02$ . The systematic uncertainty is then

$$\frac{1.024 - 1.0}{3.0 - 1.0} \times 55 \times 10^{-4} = \pm 0.7 \times 10^{-4}. \quad (6.17)$$

However, exaggerating the Bremsstrahlung also degrades the reconstruction resolution. To avoid double counting the resolution uncertainty, the contribution from the resolution must be subtracted, which results in a final Bremsstrahlung systematic uncertainty of  $\pm 0.5 \times 10^{-4}$ .

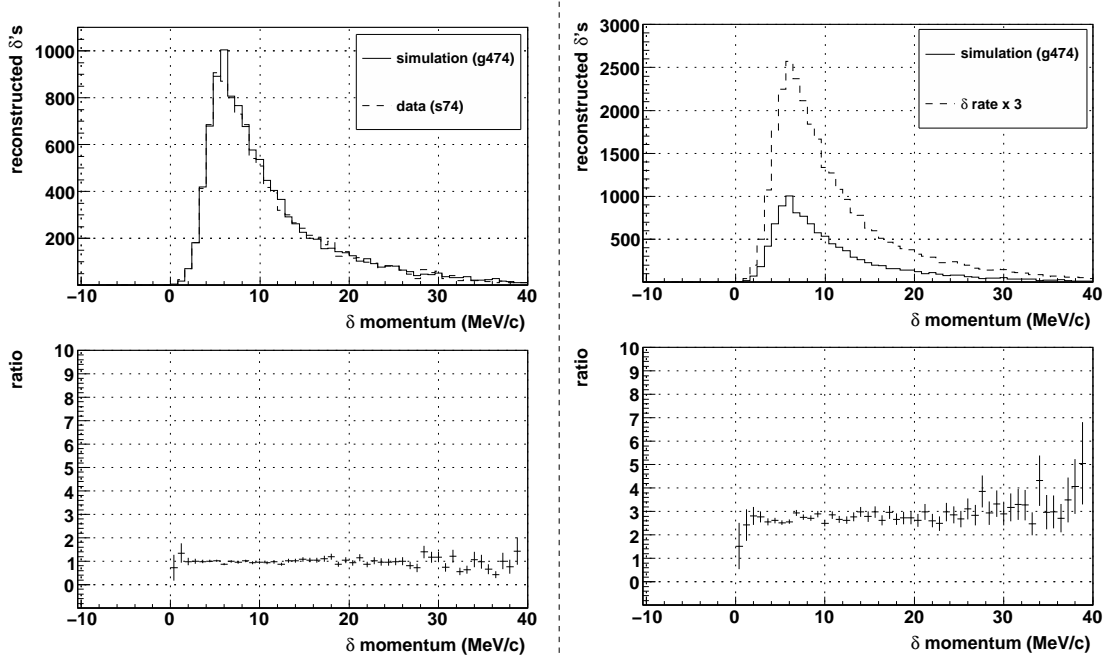


Figure 6.17: The left hand side shows the distribution of reconstructed  $\delta$ -electrons for data and simulation. The right hand side shows the simulation where the  $\delta$  production rate was increased by a factor of three. The range ( $6 < p_\delta < 16$ ) MeV/c is used to evaluate the systematic uncertainty.

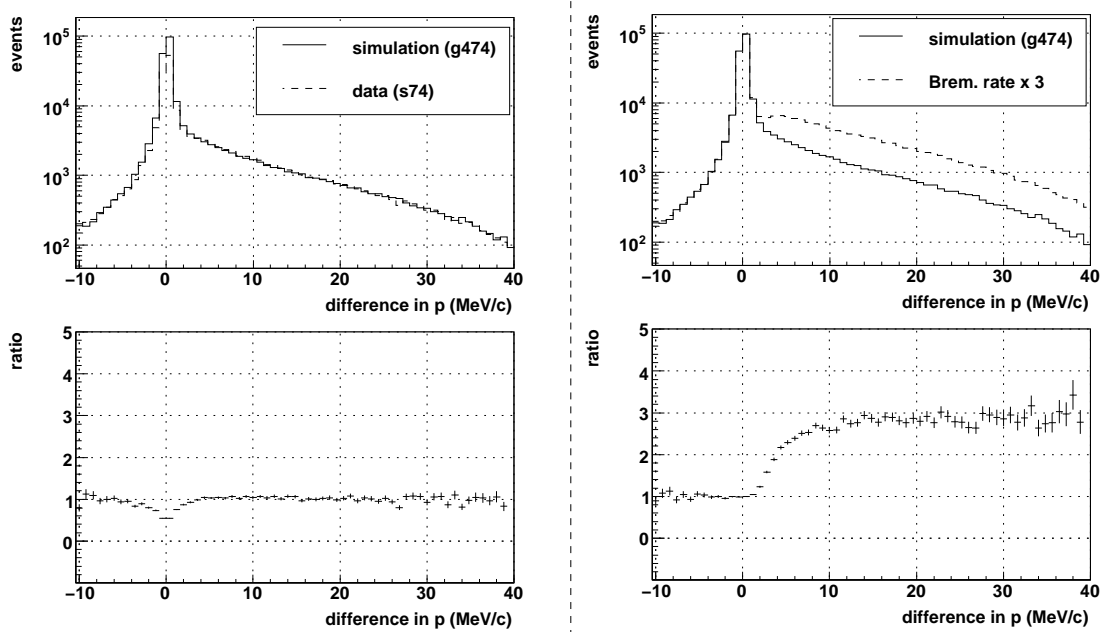


Figure 6.18: The left hand side shows the energy difference for the two halves of a broken track, for data and simulation. The right hand side shows the same distribution for a simulation where the Bremsstrahlung rate was increased by a factor of three. The range ( $15 < p < 35$ ) MeV/c is used to evaluate the systematic uncertainty.

---

## 6.5.2 Outside material

In the *upstream* half of the detector the positrons could be backscattered from the beam pipe and the upstream beam package (see Section 2.9). The door of the steel yoke was also a source of backscatters, but most of the yoke was shielded by the upstream beam package. In the *downstream* half of the detector, during nominal operation there was no corresponding downstream beam package, so positrons could only be backscattered from the steel yoke.

These backscatters cause extra hits that interfere with the decay positron reconstruction. They are well reproduced upstream in the simulation since the beam pipe and most of the upstream beam package (excluding, for example, the light guides) are included. However, the steel of the yoke is not included since the additional showering was expected to significantly increase the computation time. This lack of steel yoke and imperfections in placement and/or thickness of materials are expected to introduce a systematic uncertainty.

The degree to which backscatters match in data and simulation can be compared by selecting the time window containing the decay positron, and then finding the difference in average times between the PCs at the far upstream and downstream ends of the detector. A backscatter will cause extra hits in either the upstream or downstream PCs, resulting in an additional peak in this time distribution. The upper and middle plots in Fig. 6.19 show the time distribution for the windows where the decay positron is upstream and downstream respectively. The simulation shows evidence of a surplus in backscattered upstream decay positrons, and a deficit in backscattered downstream decay positrons that is consistent with the steel yoke being disabled.

The effect on  $P_\mu^\pi \xi$  can be estimated using two simulations, with and without the *downstream* beam package in place. This exaggerates the number of downstream decay positrons that are backscattered. The difference in  $P_\mu^\pi \xi$  between these simulations is  $(2.4 \pm 4.0) \times 10^{-4}$ , and the two time distributions are shown in the bottom panel of Fig. 6.19. The change in  $P_\mu^\pi \xi$  is then scaled down according to the ratio of differences in counts; specifically, the difference between data and simulation is divided by the difference between the simulations with and without the downstream beam package. After averaging over all sets, this results in scale factors of 7 and 14 for the upstream and downstream backscatters respectively. When added in quadrature the systematic uncertainty is then  $\sqrt{(2.4/7)^2 + (2.4/14)^2}$ , which is  $\pm 0.4 \times 10^{-4}$ .

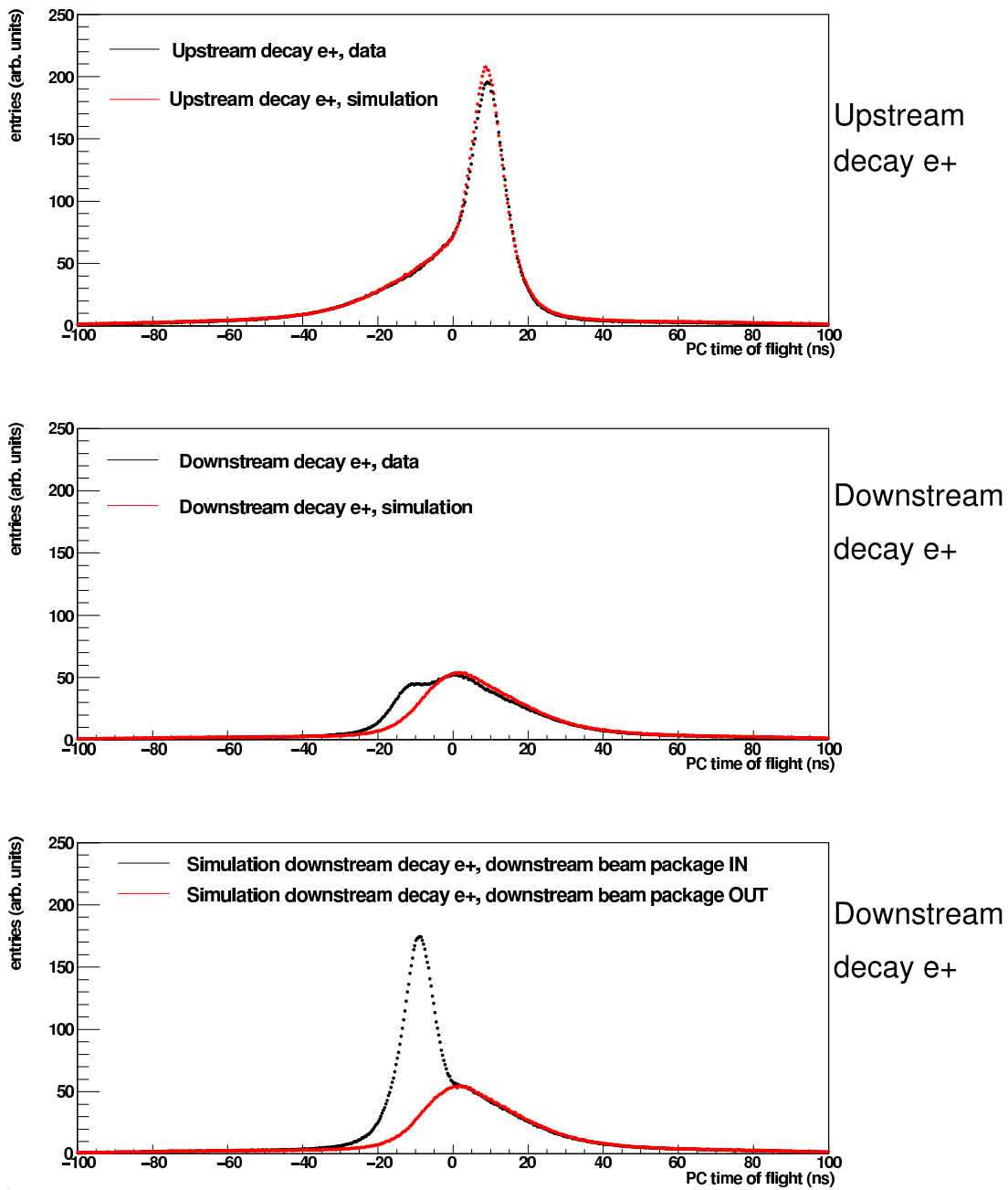


Figure 6.19: The distributions are the difference between the average upstream and downstream PC times. The backscatters from upstream and downstream decay positrons are compared for data and simulation in the upper and middle distributions. The effect of including a downstream beam package in the simulation is shown at the bottom.

---

## 6.6 Resolution

The momentum ( $p$ ) and angle ( $\cos\theta$ ) reconstruction resolutions might differ in data and simulation. This discrepancy is relatively unimportant over the kinematic fiducial since the decay spectrum is smooth. However, the analysis uses the sharp kinematic endpoint to energy calibrate the spectrum, and a significant difference in resolution at this endpoint will introduce a systematic uncertainty.

The resolution can be compared in data and simulation indirectly using special “upstream stops” data, where muons are stopped at the entrance of the detector, and the decay positron is reconstructed independently in each half of the spectrometer. The reconstructed  $p$  and  $\theta$  will differ in each half due to energy loss and multiple scattering through the target module. The distribution of the momentum/angle differences is dominated by a Gaussian resolution function, so that the difference in  $\sigma$  widths between data and simulation is a measure of how well the simulation reproduces the detector’s resolution. Even though this difference is also sensitive to discrepancies in the simulation’s positron interactions physics, we conservatively assign the full difference as a resolution problem.

The Gaussian widths are shown for a limited  $p$  range in Fig. 6.20. The absolute width is seen to depend on  $1/\sin\theta$ , but the *difference* between data and simulation is well approximated by a constant for both the momentum and angle dependence. A previous analysis found this difference in width had a non-trivial dependence on  $p$  and  $\cos\theta$ ; the current analysis is improved due to the use of superior drift cell space-time-relationships (see Section 3.2.7).

For each point in  $(p, \cos\theta)$ , the difference in  $p$  and  $\theta$  width between data and simulation is constructed according to

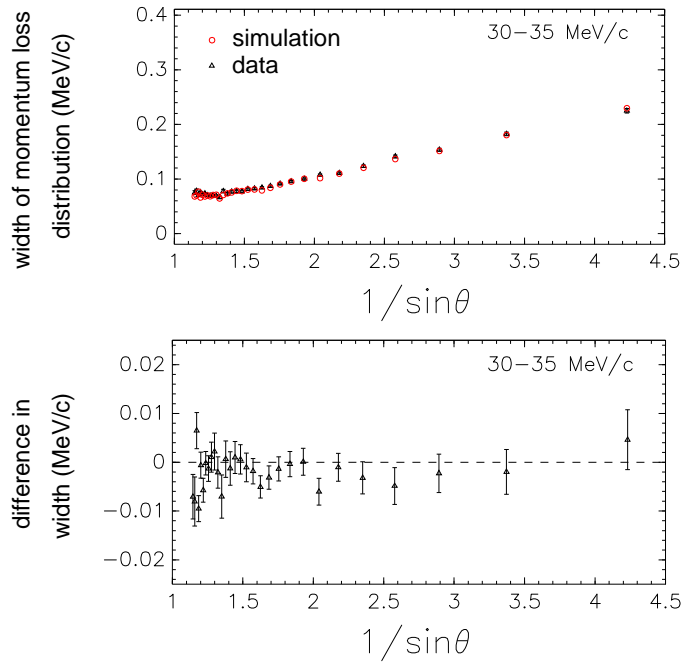
$$\Delta\sigma = \begin{cases} \sqrt{\sigma_{\text{data}}^2 - \sigma_{\text{sim}}^2} & , \sigma_{\text{data}} > \sigma_{\text{sim}} \\ -\sqrt{\sigma_{\text{sim}}^2 - \sigma_{\text{data}}^2} & , \sigma_{\text{sim}} > \sigma_{\text{data}} \end{cases} \quad (6.18)$$

The weighted average of this quantity over all  $(p, \cos\theta)$  is shown in Table 6.7. The systematic uncertainty is measured by exaggerating the largest differences from the table by a factor of five; specifically an additional smearing of 58 keV/c in momentum and 6 mrad in angle is added to the data. The momentum and angle smearing are carried out separately. The momentum smearing changes  $P_{\mu}^{\pi}\xi$  by  $(7.6 \pm 3.4) \times 10^{-4}$ , resulting in a systematic uncertainty of  $(7.6/5) \times 10^{-4} = \pm 1.5 \times 10^{-4}$ . The angle smearing changes  $P_{\mu}^{\pi}\xi$  by  $0.2 \times 10^{-4}$ , resulting in a negligible systematic uncertainty after scaling down by five.

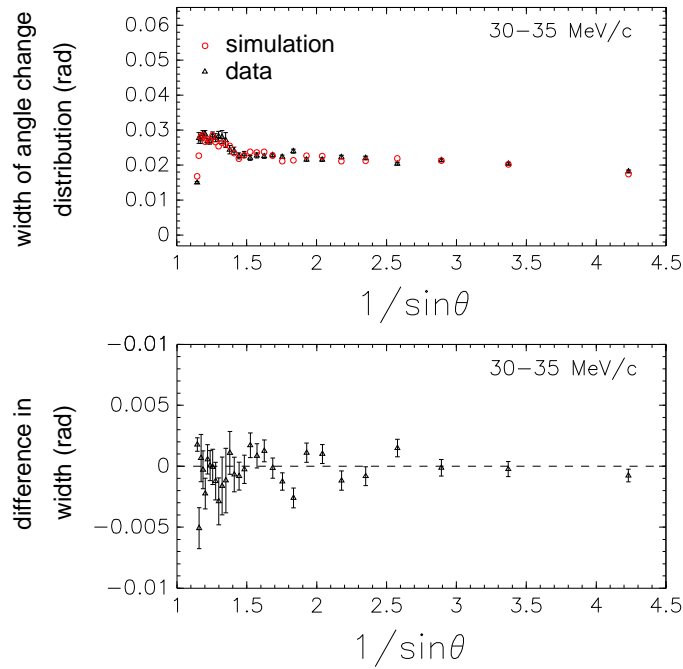
The width of the decay spectrum endpoint provides an additional independent measurement of the resolution at  $\sin \theta = 1$  (extrapolated). The data-simulation difference in this width is  $(0.0 \pm 0.3)$  keV/c for silver and  $(0.1 \pm 0.3)$  keV/c for aluminium. Since these are smaller than the differences in Table 6.7, the systematic uncertainty of  $\pm 1.5 \times 10^{-4}$  is already sufficient.

Table 6.7: Difference in resolution between data and simulation, as defined in the text.

Target	Difference in $\sigma$ , defined by Eq. (6.18)	
	Momentum (keV/c)	Angle (mrad)
Aluminium	-6.3	-0.07
Silver	-11.5	1.1



(a) Momentum resolution.



(b) Angle resolution.

Figure 6.20: Comparison of the reconstruction resolution in data and simulation, derived from a special “upstream stops” analysis: muons stop at the entrance of the detector, and are reconstructed independently in each half of the spectrometer; the width of the energy loss and angle change distributions is sensitive to the resolution.

## 6.7 Momentum calibration

### 6.7.1 Magnetic field shape

The simulation was self-consistent since it used the same `Opera` field map for generating and reconstructing the positrons. In contrast, the data were analysed with the `Opera` field map, but this had known discrepancies with the mapper measurements within the tracking region, which can introduce a systematic uncertainty.

The difference in field shape between `Opera` and the mapper measurements is well approximated by

$$\delta B_z = C_2 z^2 + C_3 z^3 + C_r r, \quad (6.19)$$

where the optimum  $C_2$ ,  $C_3$  and  $C_r$  values are recorded in Table 6.8. The three previous TWIST analyses have used the same coefficients for the nominal 2.0 T field. The coefficients were re-evaluated for the current measurement by weighting the mapper measurements more carefully[104].

Table 6.8: Coefficients of Eq. (6.19). These relate the `Opera` magnetic field to the results from the mapper measurements.

Parameter	Nominal 2.0 T field		1.96 T	2.04 T
	Previously <sup>a</sup>	<b>This analysis</b>		
$C_2$ ( $\times 10^{-8}$ T/cm <sup>2</sup> )	-6	$-1.7 \pm 0.4$	$+11.4 \pm 0.3$	$-19.7 \pm 0.5$
$C_3$ ( $\times 10^{-10}$ T/cm <sup>3</sup> )	-4	$-7.8 \pm 0.9$	$+2.0 \pm 0.5$	$-2.2 \pm 0.7$
$C_r$ ( $\times 10^{-6}$ T/cm)	-12.5	$-8.3 \pm 0.3$	$-1.1 \pm 0.6$	$-2.8 \pm 0.9$

<sup>a</sup> The same parameters were used in Refs. [57, 83, 84, 86].

A new 2.0 T field was produced with the coefficients in Eq. (6.19) exaggerated by a factor of 20. Maxwell's  $\nabla \cdot \delta \vec{B} = 0$  equation was satisfied by modifying the radial field components according to

$$\delta B_r = - \left( C_2 r z + \frac{3}{2} C_3 z^2 r \right). \quad (6.20)$$

A data set was then re-analysed with the exaggerated field, and the change in  $P_\mu^\pi \xi$  is  $(5.1 \pm 7.8) \times 10^{-4}$ . After scaling down by a factor of 20, the change in  $P_\mu^\pi \xi$  is  $0.3 \times 10^{-4}$ .

---

This is too small to justify re-analysing all the data with a corrected map, and is instead taken as a systematic uncertainty of  $\pm 0.3 \times 10^{-4}$ . Previous evaluations of this uncertainty used a smaller scale factor of ten, and did not apply Eq. (6.20), but still found an effect below  $1 \times 10^{-4}$ [57, 83].

(The data sets with a central magnetic field strength of 1.96 T and 2.04 T are not included for  $P_\mu^\pi \xi$ . Therefore the systematic due to magnetic field shape for these sets is not discussed here. See Refs. [79, 97] for further information.)

### 6.7.2 Use of the kinematic endpoint

The motivation for an energy calibration and its implementation were described in Section 3.5. In summary, the reconstructed momenta of the data and simulation disagree at the kinematic endpoints by about 10 keV/c. This difference is shown in Fig. 6.21 for the kinematic fiducial. The upstream ( $1/\cos\theta < 1$ ) and downstream ( $1/\cos\theta > 1$ ) points are fit separately with a straight line, yielding two slopes ( $a_{\text{up}}, a_{\text{down}}$ ) and two intercepts ( $b_{\text{up}}, b_{\text{down}}$ ), for a total of four “endpoint parameters”. The calibration must be applied to the entire data spectrum by shifting or scaling each reconstructed momentum. Note that the energy calibration procedure is applied to every systematic uncertainty test, which improves the robustness of the  $P_\mu^\pi \xi$  measurement.

There are three uncertainties from the energy calibration: i) a statistical part since only a limited region of the spectrum is used to establish the required correction, ii) a systematic part since either a shift or scale must be used to propagate the correction to the rest of the spectrum, and iii) a systematic part due to the model imposed on the endpoint behaviour with angle. The statistical part is propagated separately for each set, and is applied later in Section 7.1. For the systematic part due to a shift or scale, the two extremes considered were a *shift* according to

$$p_{\text{corrected}} = p_{\text{reconstructed}} - \left( b - \frac{a}{|\cos\theta|} \right), \quad (6.21)$$

and a *scale* according to

$$p_{\text{corrected}} = \frac{p_{\text{reconstructed}}}{1 + \frac{1}{W_{e\mu}} \left( b - \frac{a}{|\cos\theta|} \right)}, \quad (6.22)$$

where  $W_{e\mu}$  is the maximum kinematic positron momentum (52.83 MeV/c). The central value of  $P_\mu^\pi \xi$  is placed half way between the shift and scale extremes, and a systematic

uncertainty of half the difference is assigned to cover both possibilities ( $\pm 0.5 \times 10^{-4}$ ).

An additional systematic uncertainty is assigned due to the linear model imposed on the endpoint behaviour with  $\cos\theta$  (see Fig. 6.21). The reduced  $\chi^2$  for the linear fits average to 1.27. A decrease in the  $\chi^2$  to 1.00 corresponds to larger uncertainties for the endpoint parameters, and this ultimately results in a systematic uncertainty of  $\pm 1.4 \times 10^{-4}$  for  $P_\mu^\pi \xi$ .

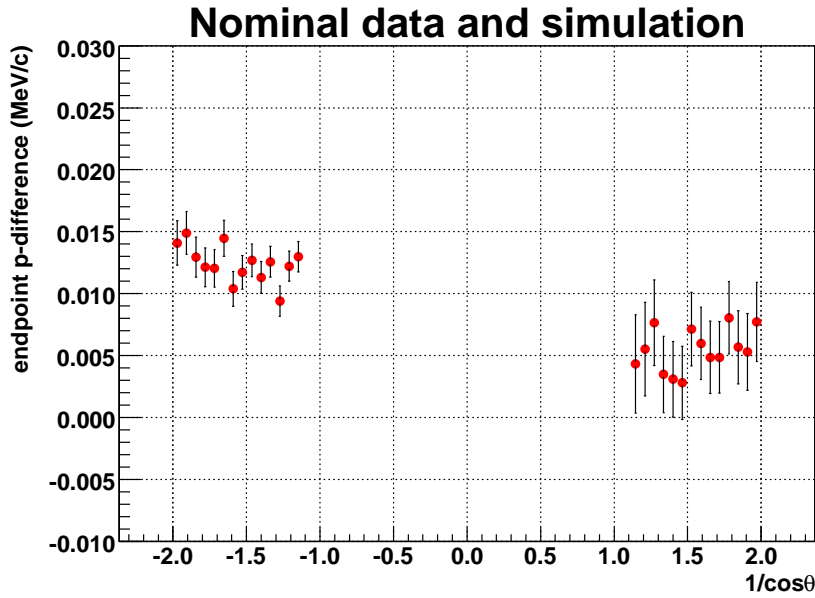


Figure 6.21: Difference between reconstructed momentum in data and simulation at the endpoint of the muon decay spectrum.

---

## 6.8 Beam stability

### 6.8.1 Muon beam intensity

The simulation's muon and beam positron rates were tuned to match the data; a disagreement can change the number of hits in the wire chambers, which affects the performance of the classification. The simulation's muon rate was tuned to match approximately the trigger rate in data. Similarly, the simulation's beam positron rate was tuned to match the probability of a beam positron entering an event.

Increasing the muon rate in the simulation by a factor of 10 changes  $\Delta P_\mu^\pi \xi$  by  $(10 \pm 7) \times 10^{-4}$ . This must be scaled down by repeating the procedure from the previous analysis[83]:

1. For each data set and its accompanying simulation, calculate the following ratio of event types:

$$R_\mu = \frac{(\text{more than one } \mu^+)}{(\text{more than one } \mu^+) + (\text{one } \mu^+, \text{ one decay } e^+)}. \quad (6.23)$$

This is a measure of the probability of an event having more than one muon.

2. Calculate the relative ratio of  $R_\mu$  for data and simulation,

$$\frac{R_\mu(\text{sim.}) - R_\mu(\text{data})}{R_\mu(\text{data})}. \quad (6.24)$$

3. Multiply the relative ratio by the average trigger rate from the data, to estimate the error (in  $\text{s}^{-1}$ ) made in the simulation.
4. Divide the simulation's error by the exaggeration ( $24579 \text{ s}^{-1}$ ).

The calculations from each of these steps appear in Table 6.9. An upper limit on the effect of data-simulation rate discrepancies uses the smallest scale factor (28.7, from set 92), resulting in a systematic uncertainty of  $(1/28.7) \times 10 \times 10^{-4} = 0.3 \times 10^{-4}$ .

The systematic uncertainty due to a beam positron rate mismatch in data and simulation is just  $\pm 0.2 \times 10^{-4}$ , and is therefore not discussed further.

Table 6.9: Scale factors for the systematic uncertainty due to beam intensity.  $R_\mu$  is a measure of the probability of an event with more than one muon. Sets 68-76 were accumulated in 2006 using a silver target. Sets 83-93 were accumulated in 2007 using an aluminium target, with a muon rate that was intentionally higher. Simulation is abbreviated as Sim.

Set	$R_\mu$ Data	$R_\mu$ Sim.	$\frac{R_\mu(\text{sim.}) - R_\mu(\text{data})}{R_\mu(\text{data})}$	Avg. data trigger ( $\text{s}^{-1}$ )	Sim. error ( $\text{s}^{-1}$ )	Scale factor
68	0.00553	0.00495	-0.10615	2066.0	-219.3	112.1
70	0.00630	0.00541	-0.14129	2324.8	-328.5	74.8
71	0.00660	0.00619	-0.06305	2582.9	-162.8	150.9
72	0.00718	0.00552	-0.23151	2674.2	-619.1	39.7
74	0.00672	0.00617	-0.08089	2592.9	-209.7	117.2
75	0.00739	0.00641	-0.13216	2686.6	-355.1	69.2
76	0.00903	0.00640	-0.29114	2740.9	-798.0	30.8
83	0.01220	0.01029	-0.15728	4221.8	-664.0	37.0
84	0.01291	0.01103	-0.14616	4452.3	-650.7	37.8
86	0.01353	0.01205	-0.10914	4972.3	-542.7	45.3
87	0.01188	0.00977	-0.17768	4024.0	-715.0	34.4
91	0.01218	0.01004	-0.17531	4202.5	-736.7	33.4
92	0.01251	0.01002	-0.19897	4305.3	-856.6	28.7
93	0.01077	0.01003	-0.06851	3809.5	-261.0	94.2

---

## 6.9 External

### 6.9.1 Radiative corrections

The simulation uses the following radiative corrections: full first order,  $O(\alpha^2 L^2)$  and  $O(\alpha^2 L^1)$  from the second order, and  $O(\alpha^3 L^3)$  from the third order. The term  $O(\alpha^2 L^0)$  was not used, despite becoming available in 2007 [16]; its effect on the decay parameters will now be shown as negligible.

Over the TWIST kinematic fiducial, the  $O(\alpha^2 L^0)$  term has a similar shape to the  $O(\alpha^2 L^1)$  term, and the ratio between the terms never exceeds 0.2; this is demonstrated in the paper where the  $O(\alpha^2 L^0)$  term is calculated[16]. The  $P_\mu^\pi \xi$  sensitivity to excluding the  $O(\alpha^2 L^0)$  term was estimated by adding a pure  $O(\alpha^2 L^1)$  spectrum to the nominal spectrum. This changes  $P_\mu^\pi \xi$  by  $(2.9 \pm 0.1) \times 10^{-4}$ . The ratio of counts in the nominal and combined spectrum is 1.11. Therefore the effect on  $P_\mu^\pi \xi$  of only adding 0.2 of the pure  $O(\alpha^2 L^1)$  spectrum is

$$(0.2/1.11) \times 2.9 \times 10^{-4} = 0.5 \times 10^{-4}, \quad (6.25)$$

and  $\pm 0.5 \times 10^{-4}$  is used as the systematic uncertainty.

### 6.9.2 Correlation with $\eta$

The muon decay spectrum does not allow a precise measurement of the parameter  $\eta$ . Therefore  $\eta$  was fixed to its world average value<sup>45</sup> of  $(-36 \pm 69) \times 10^{-4}$ [7], and the correlation between  $\eta$  and  $P_\mu^\pi \xi$  is assessed here as a systematic uncertainty. The correlation was found to be  $d\xi/d\eta = 0.01528$ , so that  $\Delta\eta = \pm 69 \times 10^{-4}$  corresponds to a  $P_\mu^\pi \xi$  systematic uncertainty of  $\pm 1.1 \times 10^{-4}$ .

---

<sup>45</sup>The evaluation of  $\eta$  in Ref. [7] uses a global analysis that includes the TWIST experiment's result for  $\rho$  and  $\delta$  from the 2002 datasets. The evaluation does *not* use the TWIST experiment's more recent  $\rho$ ,  $\delta$  and  $P_\mu^\pi \xi$  measurements from the 2004 datasets.



# Chapter 7

## Results

### 7.1 Blind results

The blind results after all corrections, including set-dependent uncertainties, are shown in Table 7.1. The uncorrected results, the corrections and the set-dependent uncertainties are listed separately in Tables 7.2 and 7.3. The results are determined independently for each of the energy calibration approaches (shift and scale) that were described in Section 6.7.2. The results for the energy calibration applied as a shift are shown in Fig. 7.1, where there is good consistency over the chosen sets. Sets 72 (TECs-in), 76 (muon beam steered in  $\theta_y$ ) and 86 (muon beam steered in  $x$  and  $\theta_x$ ) were used to evaluate the systematic uncertainty for the polarisation; they have significantly larger polarisation uncertainties that have not been evaluated, and are therefore not included in the final result. Sets 70 and 71 were taken at different central magnetic field strengths; they are excluded from the final  $P_\mu^\pi \xi$  result since the fringe field validation was only carried out at a central field strength of 2.0 T. The weighted average of  $\Delta P_\mu^\pi \xi$  is  $79.8 \times 10^{-4}$  when the energy calibration is applied as a shift, and  $80.7 \times 10^{-4}$  for a scale. Averaging over these results, and including an additional statistical uncertainty from determining the relaxation rate (see Section 6.2.10), the final blind result is

$$\Delta P_\mu^\pi \xi = [80.3 \pm 3.5 \text{ (stat.)}_{-6.3}^{+16.5} \text{ (syst.)}] \times 10^{-4}. \quad (7.1)$$

The fit quality for each set is shown in the table of uncorrected results (Table 7.2). For a nominal set, the normalised residuals are shown explicitly in Fig. 7.2. The fit quality is excellent for all sets, and there is no evidence that the normalised residuals depend on momentum or angle.

Table 7.1: Blind results, *after* all corrections, including set-dependent uncertainties.

Set	Target	Description	Shift energy calib.	Scale energy calib.
			$\Delta P_{\mu}^{\xi} (\times 10^{-4})$	$\Delta P_{\mu}^{\xi} (\times 10^{-4})$
68	Ag	Stopping distrib. peaked $\frac{1}{3}$ into target	$90.2 \pm 7.6$	$90.3 \pm 7.6$
74	Ag	Nominal A	$83.7 \pm 7.5$	$83.9 \pm 7.5$
75	Ag	Nominal B	$85.5 \pm 6.4$	$85.9 \pm 6.4$
83	Al	Downstream beam package in place	$80.7 \pm 6.6$	$82.2 \pm 6.6$
84	Al	Nominal C	$69.1 \pm 6.9$	$70.8 \pm 6.9$
87	Al	Nominal D	$82.5 \pm 6.7$	$83.6 \pm 6.7$
91	Al	Lower momentum I	$82.2 \pm 13.0$	$83.0 \pm 13.0$
92	Al	Lower momentum II	$73.5 \pm 11.2$	$75.0 \pm 11.2$
93	Al	Lower momentum III	$62.1 \pm 9.2$	$63.8 \pm 9.2$
70	Ag	B = 1.96 T	$79.0 \pm 6.3$	$80.0 \pm 6.3$
71	Ag	B = 2.04 T	$93.2 \pm 6.6$	$93.3 \pm 6.6$
72	Ag	TECs-in, nominal beam	$90.7 \pm 6.4$	$91.1 \pm 6.4$
76	Ag	Steered beam A	$33.2 \pm 7.0$	$33.6 \pm 7.0$
86	Al	Steered beam B	$52.7 \pm 6.2$	$54.6 \pm 6.2$

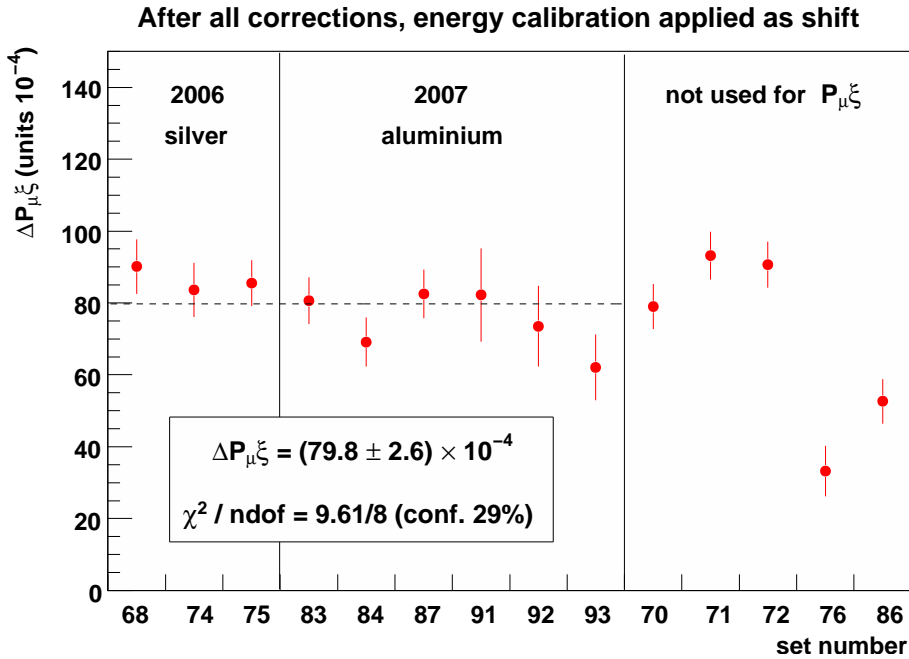

 Figure 7.1: Consistency of  $\Delta P_{\mu}^{\pi\xi}$ , the difference in  $P_{\mu}^{\pi\xi}$  between the data and a hidden value in the simulation.

Table 7.2: Blind results, *before* any corrections.

Set	Energy calibration applied as a shift			Energy calibration applied as a scale		
	$\chi^2/\text{ndf}$	Confidence	$\Delta P_\mu \xi (\times 10^{-4})$	$\chi^2/\text{ndf}$	Confidence	$\Delta P_\mu \xi (\times 10^{-4})$
68	2384/2439	78.3	$84.9 \pm 7.6$	2373/2439	82.7	$84.9 \pm 7.6$
74	2440/2439	49.3	$78.3 \pm 7.5$	2450/2439	43.7	$78.5 \pm 7.5$
75	2453/2439	41.8	$80.6 \pm 6.4$	2452/2439	42.2	$80.8 \pm 6.4$
83	2405/2439	68.5	$75.3 \pm 6.5$	2416/2439	62.5	$76.8 \pm 6.5$
84	2515/2439	13.8	$63.6 \pm 6.8$	2510/2439	15.4	$65.2 \pm 6.8$
87	2411/2439	65.5	$77.1 \pm 6.7$	2407/2439	67.6	$78.1 \pm 6.7$
91	2564/2439	3.9	$71.4 \pm 12.9$	2578/2439	2.5	$72.0 \pm 12.9$
92	2474/2439	30.7	$63.3 \pm 11.1$	2479/2439	28.2	$64.7 \pm 11.1$
93	2504/2439	17.4	$52.5 \pm 9.0$	2518/2439	13.1	$54.1 \pm 9.0$
70	2370/2439	84.0	$74.0 \pm 6.3$	2380/2439	80.0	$74.9 \pm 6.3$
71	2425/2439	57.6	$88.1 \pm 6.6$	2430/2439	54.9	$88.1 \pm 6.6$
72	2513/2439	14.4	$85.8 \pm 6.4$	2508/2439	16.3	$86.2 \pm 6.4$
76	2430/2439	55.2	$27.5 \pm 7.0$	2423/2439	58.9	$27.8 \pm 7.0$
86	2425/2439	57.7	$47.7 \pm 6.2$	2424/2439	58.0	$49.6 \pm 6.2$

Table 7.3: Set-dependent corrections and uncertainties for  $\Delta P_\mu^\pi \xi$ . These are described in Section 6.1.

Set	Corrections (units $10^{-4}$ )					Set-dependent uncertainties (units $10^{-4}$ )	
	Production target	Relaxation rate	Spectrum fitter	Energy calib. Scale	Energy calib. Shift	Energy calib. statistical	Production target
68	+0.9	+2.7	-0.5	+2.2	+2.3	$\pm 0.5$	$\pm 0.3$
74	+0.9	+2.7	-0.5	+2.3	+2.4	$\pm 0.5$	$\pm 0.3$
75	+0.9	+2.7	-0.5	+1.9	+2.0	$\pm 0.4$	$\pm 0.3$
83	+0.9	+3.3	-0.5	+1.7	+1.8	$\pm 0.4$	$\pm 0.3$
84	+0.9	+3.3	-0.5	+1.8	+1.9	$\pm 0.4$	$\pm 0.3$
87	+0.9	+3.3	-0.5	+1.8	+1.9	$\pm 0.4$	$\pm 0.3$
91	+5.9	+3.3	-0.5	+2.1	+2.2	$\pm 0.9$	$\pm 1.9$
92	+5.2	+3.3	-0.5	+2.2	+2.4	$\pm 0.7$	$\pm 1.6$
93	+5.2	+3.3	-0.5	+1.7	+1.7	$\pm 0.6$	$\pm 1.6$
70	+0.9	+2.7	-0.5	+1.9	+2.0	$\pm 0.4$	$\pm 0.3$
71	+0.9	+2.7	-0.5	+2.0	+2.1	$\pm 0.4$	$\pm 0.3$
72	+0.9	+2.7	-0.5	+1.8	+1.9	$\pm 0.4$	$\pm 0.3$
76	+0.9	+3.3	-0.5	+2.1	+2.2	$\pm 0.4$	$\pm 0.3$
86	+0.9	+3.3	-0.5	+1.3	+1.4	$\pm 0.4$	$\pm 0.3$

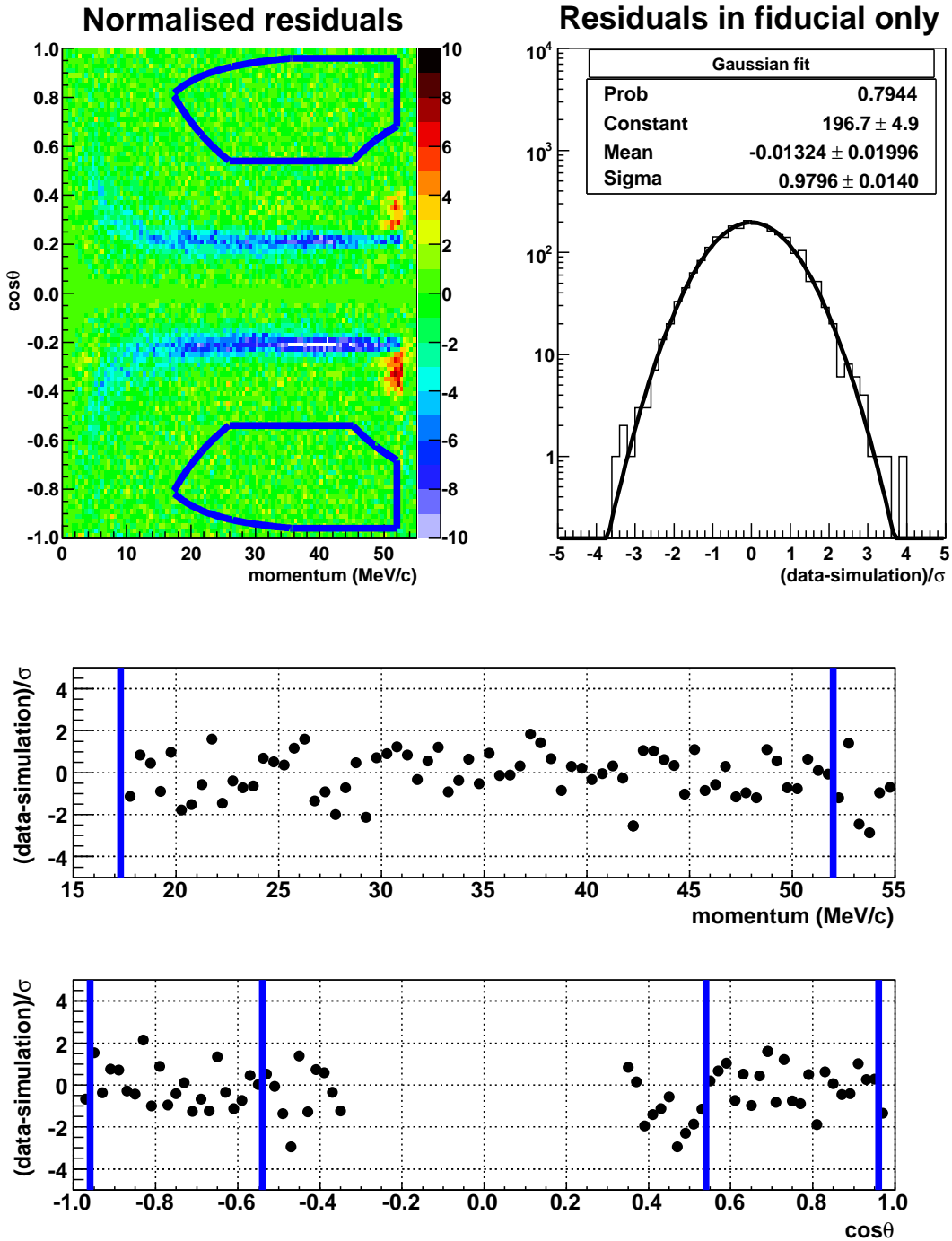


Figure 7.2: Normalised residuals from a spectrum fit of nominal data (set 87) to its accompanying simulation. The thick blue lines indicate the kinematic fiducial boundaries. Within the fiducial region there is no evidence of structure.

---

## 7.2 Result revealed

On 29 January 2010, the hidden value of  $\xi$  was revealed as

$$\xi_{\text{hidden}} = 0.99281. \quad (7.2)$$

This is added to the blind result in Eq. (7.1) to give

$$P_{\mu}^{\pi} \xi = 1.00084 \pm 0.00035 \text{ (stat.)}_{-0.00063}^{+0.00165} \text{ (syst.)}, \quad (7.3)$$

which agrees with all previous results for  $P_{\mu}^{\pi} \xi$  and  $P_{\mu}^K \xi$ , and is consistent with the standard model values of  $P_{\mu}^{\pi} = \xi = 1$ . The new result is a factor of 3.2 more precise than the previous TWIST measurement,  $P_{\mu}^{\pi} \xi = 1.0003 \pm 0.0006 \text{ (stat.)} \pm 0.0038 \text{ (syst.)}$ [21], and a factor of 7.0 more precise<sup>46</sup> than the pre-TWIST direct measurement,  $P_{\mu}^{\pi} \xi = 1.0027 \pm 0.0079 \text{ (stat.)} \pm 0.0030 \text{ (syst.)}$ [67]. The new result is also compatible with a recent *indirect* measurement that used TWIST  $\rho$  and  $\delta$  results,  $0.99524 < P_{\mu} \xi \leq \xi < 1.00091$  (90% C.L.)[10]. Note that Eq. (7.3) is the final result of the TWIST  $P_{\mu}^{\pi} \xi$  blind analysis, and this number will be published.

## 7.3 “White box” consistency test

A simulation was generated using the final result in Eq. (7.3) for  $\xi$ . The resulting spectrum was fit against the data. After applying all corrections, the result must come out consistent with zero for the consistency test to be passed. This has been carried out twice (once for the silver target, and once for aluminium), and the results are

$$\Delta P_{\mu}^{\pi} \xi (\text{Ag}) = (-7.9 \pm 7.5) \times 10^{-4}, \quad (7.4)$$

$$\Delta P_{\mu}^{\pi} \xi (\text{Al}) = (+7.2 \pm 6.9) \times 10^{-4}. \quad (7.5)$$

These are consistent with zero, which confirms that all corrections have been applied properly.

---

<sup>46</sup>In units of  $10^{-4}$ , the uncertainty corresponding to  $\pm$  one standard deviation for the pre-TWIST direct measurement is  $2 \times \sqrt{79^2 + 30^2} = 169$ . For the current measurement, the positive error bar is  $\sqrt{3.5^2 + 16.5^2} = 16.9$ , and the negative error bar is  $\sqrt{3.5^2 + 6.3^2} = 7.2$ , giving the size of  $\pm$  one standard deviation as  $16.9 + 7.2 = 24.1$ . The improvement factor is then  $169/24.1 = 7.0$ .

## 7.4 Physics implications

The  $P_\mu^\pi \xi$  result will be used in a global analysis, as described in Section 1.4.2. At the time of writing this analysis is not yet available in a final form, and hence it will not be discussed here.

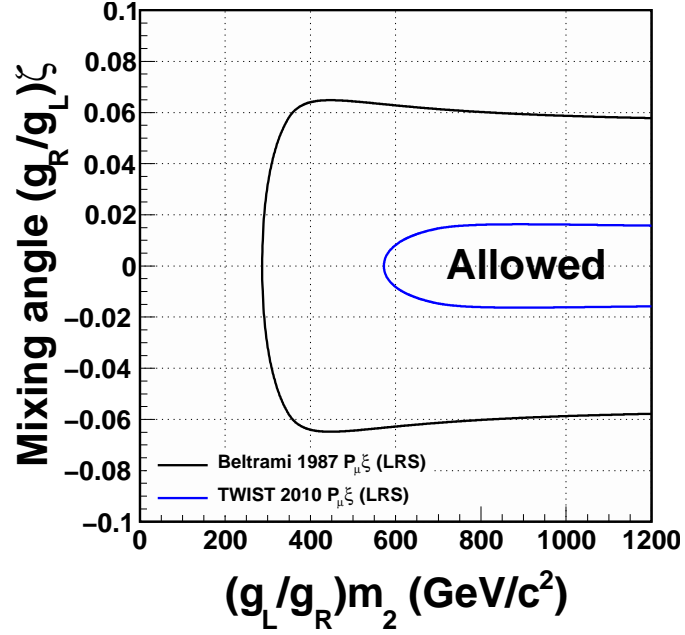
Several left-right symmetric (LRS) models were described in Section 1.5.2. The most restrictive is the manifest LRS model, where the weak coupling constants and CKM matrices are the same for left- and right-handed particles, and there is no CP violating phase. The generalised LRS model relaxes all of these requirements. An exclusion region for the manifest and generalised LRS models can be constructed at the 90% confidence level. After enforcing the requirement in the LRS models that  $P_\mu^\pi \xi \leq 1$ , the lower limit at 90% confidence is  $[P_\mu^\pi \xi]_{90} = 0.99922$ . This value is used in Eqs. (1.27)-(1.32) to produce Fig. 7.3, which compares the pre-TWIST direct  $P_\mu^\pi \xi$  result with the value from the current analysis. In the generalised LRS model, the lower limit for an additional W-boson mass is increased from  $(g_L/g_R)m_2 = 287 \text{ GeV}/c^2$  to  $573 \text{ GeV}/c^2$ , and in the manifest LRS, the lower limit is increased from  $m_2 = 318 \text{ GeV}/c^2$  to  $573 \text{ GeV}/c^2$ . Note that Fig. 7.3 should not be used as the final TWIST exclusion region; a future publication will include the effect of the new TWIST  $\rho$  measurement, and will likely result in a more restrictive plot.

## 7.5 Future experiments

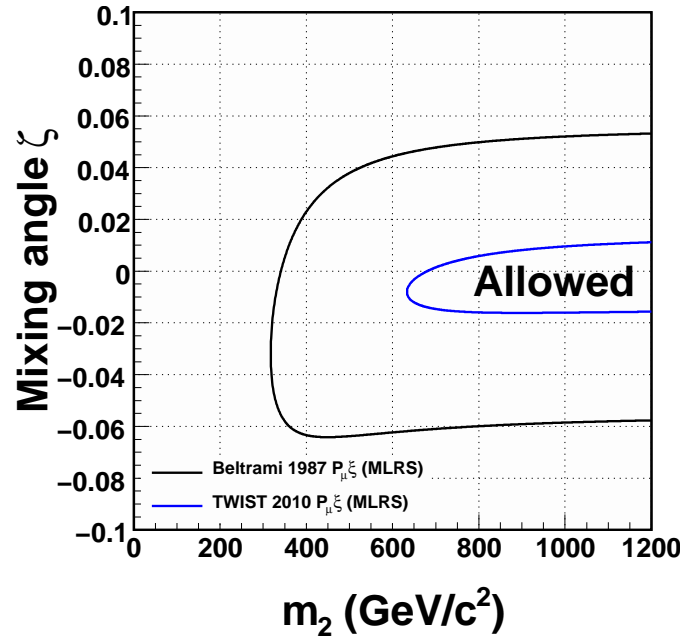
A  $P_\mu^\pi \xi$  measurement with precision greater than  $1 \times 10^{-4}$  is possible with a TWIST-style experiment (*i.e.* longitudinally polarised muons delivered into the centre of uniform magnetic field, with high precision positron tracking). The uncertainties that limited the current measurement will be briefly discussed, with a view to how they could be reduced.

### 7.5.1 Statistical uncertainty

The statistical uncertainty for this measurement is already at the level of  $3.5 \times 10^{-4}$ , or just  $2.5 \times 10^{-4}$  for the part that originates from the decay spectrum fit. This was achieved with about four months of continuous data acquisition at a surface muon rate of  $2000 - 5000 \text{ s}^{-1}$  (a significant amount of tuning over the years 2000 to 2006 was necessary to achieve the required beam quality). The statistical uncertainty of a future measurement could be reduced to commensurate levels by using a channel with an order of magnitude



(a) Generalised LRS model.



(b) Manifest LRS model.

Figure 7.3: Exclusion region (90% confidence limit) for  $\zeta$ , the mixing angle between the left- and right-handed  $W$ -boson eigenstates, and  $(g_L/g_R)m_2$ , where  $g_L$  and  $g_R$  are the weak coupling constants for the predominantly left and right-handed  $W$ -bosons, and  $m_2$  is the mass of the predominantly right-handed  $W$ -boson. The “Beltrami” entry refers to the pre-TWIST direct  $P_\mu^\pi \xi$  measurement[67].

higher flux. For example, a new  $\mu$ E4 channel at PSI already achieves this by placing radiation-hard solenoids close to the muon production target, allowing an acceptance of  $\Delta\Omega \sim 135$  msr[81] compared to 29 msr from the M13 beam line. A higher rate would require an improvement in the data acquisition electronics, in order to prevent significant pileup. If the TWIST analysis approach were adopted, using an accompanying simulation to include inefficiencies and biases, then the simulation statistics could be significantly increased by taking advantage of faster CPUs.

### 7.5.2 Magnetic field map uncertainty

The dominant systematic uncertainty from the fringe field could be reduced. We used an MRI magnet surrounded by a custom steel yoke, but a specially constructed magnet could provide a more gradual fringe field by increasing the  $z$ -distance over which the field reaches its full strength. Alternatively, or additionally, a higher-rate muon channel would allow the possibility of beam collimation; by selecting low angle muons that undergo very little depolarisation, the uncertainty on that depolarisation would be decreased. However, such collimators could introduce an additional uncertainty from muons scattering off them, and this would have to be carefully assessed; active collimation may help to reduce problems.

The measurement of our magnetic field could have been done better. A future experiment would need alignments of the measuring apparatus under control at the  $< 0.5$  mm and  $< 1$  mrad level, and should measure all three components of the magnetic field. If the three components are measured with more than one probe, then the relative orientation of the probes must be known with high precision, and a correction may be necessary for the probes not being at exactly the same point in space; a smaller field gradient would also help here. Also, the current experiment would have benefited from field measurements at finer spaced intervals (in all coordinates) over the region that the muons actually traversed.

We used the `Opera` magnetic field simulation to produce the  $B_x$  and  $B_y$  components of our field map. With all three components measured, it may not be necessary to have a magnetic field simulation at all, although an alternative method of smoothing the field measurements would be necessary. If a simulation is required, it is recommended that more than one piece of software be used; for example, the latest version of `Opera`[85], or the COMSOL Multiphysics (formerly FEMLAB) software[105].

The TWIST approach was to measure the muons before the fringe field, and rely on a `GEANT3` simulation to predict the final polarisation. There are at least two ways to

---

improve the confidence in the final polarisation: first the spin could be transported by one or more independent simulations; second the beam could be steered off-axis in order to lower the polarisation, and a simulation’s ability to reproduce the polarisation change from the data would allow confidence to be gained. As seen in this thesis, the alignment of the beam and the field must be under strict control in order for the second approach to work.

The time expansion chambers (TECs) that measured our muon beam had adequate precision, but suffered from alignment uncertainties and aging problems that would be more significant for a future measurement. An improved measurement using a similar device would have to address these issues. A significant uncertainty from the TECs originated from the simulation’s ability to correct for the multiple scattering that takes place while the muons pass through the active volume; a subsidiary experiment may be needed to validate the simulation’s accuracy in making this correction.

An alternative proposal put forward by a TWIST collaborator is to measure the muon beam inside the strong magnetic field[106, 107]. This would present a greater engineering and analysis challenge, since the device would have to work in a strong magnetic field and the reconstructed trajectories would be helices. If carried out accurately, this approach has the potential to eliminate many of the problems associated with simulating the spin.

### 7.5.3 Stopping material depolarisation uncertainty

For the current measurement the polarisation’s relaxation rate was measured using the normal data. A subsidiary  $\mu^+$ SR experiment provided a consistent but uncompetitive result. A future experiment should consider an integrated “ $\mu^+$ SR mode”, with a higher beam intensity and a simple analysis that only identifies particles and their times. The goal should be to unequivocally determine the form of  $P_\mu(t)$  and its parameters. Since this experimental mode would not measure the absolute polarisation, a Wien filter should be considered to significantly reduce the beam positrons, which would allow a much higher muon rate. (A  $\mu^+$ SR analysis was considered using the existing TWIST detector. The proportional chambers (PCs) had a timing resolution of  $\sim 20$  ns, and could identify particles based on their pulse width. This would have allowed us to use decay data below  $1 \mu\text{s}$  to better determine the relaxation rate. However, the suggestion came at a late stage in the analysis and would have required significant software changes to implement.)

If a “ $\mu^+$ SR mode” is not possible, then a subsidiary  $\mu^+$ SR experiment should be considered from the outset. Suggestions are made in Section H.9 that would allow a better

time differential  $\mu^+$ SR measurement. Another useful measurement could be provided by a pulsed muon setup such as that of the Rutherford Appleton Laboratory (UK).

For the TWIST polarisation measurements, only aluminium and silver targets were used. Additional targets that produced consistent  $P_\mu^\pi \xi$  measurements would strengthen a future result.

We were able to successfully eliminate muons that stopped in the gas before our stopping target; a stricter cut could have further reduced the contamination, with a loss of statistical precision. However, one surprise was our simulation's prediction that 0.11% of muons passed through the metal stopping target and entered PC7, and did not have enough energy to produce a signal. A more careful simulation of the PC response would have allowed us to determine this fraction better, and correct  $P_\mu^\pi \xi$  accordingly.

#### 7.5.4 Other uncertainties

The uncertainty from production target scattering can be reduced in three ways: i) by selecting a smaller momentum resolution, which would be feasible with a higher intensity beam line, ii) by a more accurate validation of the multiple scattering within the simulation, iii) if one could select a wide range of sub-surface muon momenta, then muons from much deeper within the production target could be selected; the difference in polarisation between the lower momentum muons and the surface muons would then help to validate the simulation of multiple scattering.

There are theoretical considerations at the  $< 1 \times 10^{-4}$  level that would be important for future measurements. The next level of radiative corrections (full  $O(\alpha^3)$ ) would ideally be evaluated. A calculation of radiative corrections that does not assume an underlying ( $V - A$ ) interaction would be very welcome, although this would need a suitable renormalisable theory. The pion radiative decay mode should also be considered more carefully; such calculations have been carried out for the purposes of TWIST[108].

The track reconstruction efficiency and resolution were both measured here using a special analysis with the muons stopped at the entrance of the spectrometer, and the decay positron reconstructed separately in each half of the detector. A future experiment should consider designing the beam line to allow a “spread muon tune”, where the muons stop close to the detector entrance but are spread out over a much wider area than usual. In addition, the stopping target should be as large as possible to allow a wide range of decay positron phase space to be reconstructed in each detector half. Also the ability to rotate the entire detector (*i.e.* swap the upstream and downstream ends) would provide a

---

more stringent test of measurements that compare the upstream and downstream response of the detector.

The uncertainties from positron interactions (mostly  $\delta$ -electrons and bremsstrahlung) will need careful consideration. This may require work by theorists, or a comparison of several simulations that claim to accurately reproduce these processes in the relevant energy range. A future experimenter should consider a subsidiary experiment to help understand these processes better in the low energy range.

Another area requiring thought is the energy calibration. Inevitably a correction or calibration will be needed since the decay positron reconstruction will have subtle biases and systematic errors. The method of measuring and then propagating such a correction will likely be dominant in a future  $P_\mu^\pi \xi$  measurement. For the TWIST experiment this correction was due to a complex combination of errors in the magnetic field map, imperfect drift cell space-time-relationships, bias from the helix fitting, the energy-loss model in the simulation, multiple scattering of the decay positron and uncertainties in the stopping distribution; these pieces could not be disentangled, and, as a result, a conservative approach was taken in the propagation of the energy calibration to the bulk of the decay spectrum. A future experiment must consider ways of eliminating these errors, or breaking them into orthogonal pieces; see Ref. [97] for more information.

The remaining uncertainties from Table 6.1 could have easily been reduced. The beam intensity uncertainty could be eliminated by tuning the simulation's muon rate to properly match the data, using the  $R_\mu$  criteria described in Section 6.8.1. The uncertainty from background muons could be reduced by tuning the stopping distribution based on the  $\alpha_{\text{diff}}$  criteria in Section 6.2.12, and/or adding to the simulation a source of pions at the end of the M13 beam line. The refined space-time-relationships in the DCs and the wire time offsets were already adequate for a measurement at the  $< 1 \times 10^{-4}$  level. The strict engineering requirements of the TWIST detector meant that alignment uncertainties were already at a negligible level. The outside material systematic could be eliminated by adding more detail to the geometry of the simulation outside of the active detector region. The  $\eta$  correlation will be reduced for future measurements after a global analysis using this  $P_\mu^\pi \xi$  measurement and the simultaneous  $\rho$  and  $\delta$  measurements.

In addition to the goal of extracting  $P_\mu^\pi \xi$  (and  $\rho$ ,  $\delta$ ), a future experiment should consider subsidiary measurements that may even benefit the main experiment. An  $\eta$  measurement from the decay spectrum would provide a validation of the results that use the transverse polarisation of the decay positron, although positron interactions would have to be thoroughly understood since  $\eta$  affects the low momentum end of the spectrum.

Some extensions to the standard model postulate additional parameters to describe the decay spectrum; see Ref. [79] for a more detailed discussion. The *negative* muon decay spectrum for each stopping target could be produced using the same analysis software; see Ref. [109] for such a measurement (the first of its kind) that used the TWIST apparatus. Lastly, if there was a possibility to switch between muons sourced from pions and kaons, then the resulting  $P_\mu^\pi \xi$  and  $P_\mu^K \xi$  measurements would provide a more complete test of the standard model.

## 7.6 Conclusions

The quantity  $P_\mu^\pi \xi$  has been measured as

$$P_\mu^\pi \xi = 1.00084 \pm 0.00035 \text{ (stat.)}_{-0.00063}^{+0.00165} \text{ (syst.)}. \quad (7.6)$$

This is the final direct  $P_\mu^\pi \xi$  measurement from the TWIST collaboration, and is a factor of 7.0 more precise than the pre-TWIST result [67]. The result improves the limits on the mass of an additional right-handed W-boson in left-right symmetric models, and will be used to limit extensions to the standard model in a global analysis of muon decay data.

# Bibliography

- [1] S. Weinberg. A Model of Leptons. *Phys. Rev. Lett.*, 19(21):1264–1266, Nov 1967.
- [2] Donald Hill Perkins. *Introduction to High-Energy Physics; 4th ed.* Cambridge Univ. Press, Cambridge, 2000.
- [3] C. Amsler *et al.* Review of Particle Physics. *Phys. Lett. B*, 667(1-5):1–6, 2008. Review of Particle Physics.
- [4] D. Griffiths. *Introduction to Elementary Particles.* Wiley, 1987.
- [5] M. Goldhaber, L. Grodzins, and A. W. Sunyar. Helicity of Neutrinos. *Phys. Rev.*, 109:1015 – 1017, 1958.
- [6] D. Binosi and L. Theußl (sic.). JaxoDraw: A graphical user interface for drawing Feynman diagrams. *Comput. Phys. Commun.*, 161:76–86, August 2004.
- [7] C.A. Gagliardi, R.E. Tribble and N.J. Williams. Global analysis of muon decay measurements. *Phys. Rev. D*, 72(7):073002, Oct 2005.
- [8] W. Fetscher, H.-J. Gerber and K.F. Johnson. Muon decay: complete determination of the interaction and comparison with the standard model. *Phys. Lett. B*, 173(1):102–106, 1986.
- [9] S. Eidelman *et al.* Review of Particle Physics. *Phys. Lett. B*, 592(1-4):1–5, 2004. Review of Particle Physics.
- [10] R.P. MacDonald *et al.* Precision measurement of the muon decay parameters  $\rho$  and  $\delta$ . *Phys. Rev. D*, 78(3):032010, 2008.
- [11] A. Sirlin, New York University, USA. Private communication.
- [12] A. B. Arbuzov. First-order radiative corrections to polarized muon decay spectrum. *Phys. Lett. B*, 524(1-2):99 – 106, 2002.

- [13] A. Arbuzov, A. Czarnecki and A. Gaponenko. Muon decay spectrum: Leading logarithmic approximation. *Phys. Rev. D*, 65:113006, 2002.
- [14] A. Arbuzov and K. Melnikov.  $\mathcal{O}(\alpha^2 \ln(m_\mu/m_e))$  corrections to electron energy spectrum in muon decay. *Phys. Rev. D*, 66:093003, 2002.
- [15] A. Arbuzov. Higher order QED corrections to muon decay spectrum. *J. High Energy Phys.*, 2003(03):063–063, 2003.
- [16] K. Melnikov C. Anastasiou and F. Petriello. The electron energy spectrum in muon decay through  $\mathcal{O}(\alpha^2)$ . *J. High Energy Phys.*, (09):014, 2007.
- [17] N. Danneberg *et al.* Muon Decay: Measurement of the Transverse Polarization of the Decay Positrons and its Implications for the Fermi Coupling Constant and Time Reversal Invariance. *Phys. Rev. Lett.*, 94:021802, 2005.
- [18] C. Gagliardi, Texas A&M University, Texas, USA. Private communication.
- [19] P. Herczeg. On muon decay in left-right-symmetric electroweak models. *Phys. Rev. D*, 34(11):3449–3456, Dec 1986.
- [20] V.M. Abazon *et al.* Search for  $W'$  Bosons Decaying to an Electron and a Neutrino with the D0 Detector. *Phys. Rev. Lett.*, 100:031804, 2008.
- [21] B. Jamieson *et al.* Measurement of  $P_\mu \xi$  in polarized muon decay. *Phys. Rev. D*, 74(7):072007, 2006.
- [22] J.D. Jackson. *Classical Electrodynamics*. John Wiley & Sons, 1999.
- [23] V. Bargmann, L. Michel and V.L. Telegdi. Precession of the Polarization of Particles Moving in a Homogeneous Electromagnetic Field. *Phys. Rev. Lett.*, 2:435–436, 1959.
- [24] A. Balakin, V. Kurbanova and W. Zimdahl. Precession of a particle with anomalous magnetic moment in electromagnetic and gravitational pp-wave fields. *Gravity Cosmology Supplement*, 82:6–9, 2002.
- [25] P. Depommier. The BMT equation. Presentation to TWIST collaboration, May 2006.
- [26] P. Depommier. Muon depolarization in multiple scattering (TN100). Technical report, TWIST collaboration, TRIUMF, 2005.

- 
- [27] W.H. Koppenol. Names for muonium and hydrogen atoms and their ions(IUPAC Recommendations 2001). *Pure Appl. Chem.*, 73:377–379, 2001.
- [28] M. Senba. Muon spin depolarization in noble gases during slowing down in a longitudinal magnetic field. *J. Phys. B: At. Mol. Opt. Phys.*, 31:5233–5260, 1998.
- [29] A. Jodidio *et al.* Search for right-handed currents in muon decay. *Phys. Rev. D*, 34(7), 1986.
- [30] A. Jodidio *et al.* Erratum: Search for right-handed currents in muon decay. *Phys. Rev. D*, 37(1), 1988.
- [31] J. H. Brewer. Muon spin rotation/relaxation/resonance. In *Encyclopedia of Applied Physics 11*, pages 23–53. 1994.
- [32] S.F.J. Cox. Implanted muon studies in condensed matter science. *J. Phys. C: Solid State Phys*, 20:3187–3319, 1987.
- [33] O. Hartmann *et al.* Diffusion of positive muons in some cubic metals. *Phys. Lett. A*, 61(2):141 – 142, 1977.
- [34] J. Brewer, University of British Columbia, Canada. Private communication.
- [35] W.B. Gauster *et al.* Measurement of the depolarization rate of positive muons in copper and aluminum. *Solid State Commun.*, 24(9):619–622, 1977.
- [36] W. Schilling. The physics of radiation damage in metals. *Hyperfine Interact.*, 4:636–644, 1978.
- [37] D.K. Brice. Lattice atom displacements produced near the end of implanted  $\mu^+$  tracks. *Phys. Lett. A*, 66:53–56, 1978.
- [38] P. Dalmas de Réotier and A. Yaouanc. Muon spin rotation and relaxation in magnetic materials. *J.Phys: Condens. Matter*, 9:9113–9166, 1997.
- [39] P. Dalmas de Réotier and A. Yaouanc. Quantum calculation of the muon depolarization function: effect of spin dynamics in nuclear dipole systems. *J.Phys: Condens. Matter*, 4:4533–4556, 1992.
- [40] A. Abragam. *Principles of Nuclear Magnetism*. International series of monographs on physics. Oxford University Press, 1986.

- [41] R.S. Hayano *et al.* Zero- and low-field spin relaxation studied by positive muons. *Phys. Rev. B*, 20:850, 1979.
- [42] W.J. Kossler *et al.* Diffusion and Trapping of Positive Muons in Al:Cu Alloys and in Deformed Al. *Phys. Rev. Lett.*, 41:1558–1561, 1978.
- [43] O. Hartmann *et al.* Coherent Propagation and Strain-Induced Localization of Muons in Al. *Phys. Rev. Lett.*, 41:1055–1058, 1978.
- [44] K.W. Kehr *et al.* Muon diffusion and trapping in aluminum and dilute aluminum alloys: Experiments and comparison with small-polaron theory. *Phys. Rev. B*, 26:567–589, 1982.
- [45] K.W. Kehr. Empirical information on quantum diffusion. *Hyperfine Interact.*, 17-19:63–74, 1984.
- [46] O. Hartmann. Diffusion and trapping of muons in aluminum: New experiments and comparison with Kondo theory. *Phys. Rev. B*, 37:4425–4440, 1988.
- [47] O. Hartmann. New results on diffusion in fcc metals. *Hyperfine Interact.*, 64:641–648, 1990.
- [48] O. Hartmann *et al.* Studies of  $\mu^+$  Localization in Cu, Al, and Al alloys in the Temperature Interval 0.03 – 100 K. *Phys. Rev. Lett.*, 44:337–340, 1980.
- [49] D.P. Stoker *et al.* Search for Right-Handed Currents by Means of Muon Spin Rotation. *Phys. Rev. Lett.*, 54:1887–1890, 1985.
- [50] D.P. Stoker, University of California, Irvine, USA. Private communication.
- [51] J. Korrynga. Nuclear magnetic relaxation and resonance (sic.) line shift in metals. *Physica*, 7-8:601–610, 1950.
- [52] S.J. Blundell and S.F.J. Cox. Longitudinal muon spin relaxation in metals and semimetals and the Korringa law. *J. Phys.: Condens. Matter*, 13:2163–2168, 2001.
- [53] J.H. Brewer *et al.* *Positive muons and muonium in matter*. Muon Physics. Academic Press Inc (London) Limited, 1975.
- [54] S.F.J. Cox *et al.* Muon Korringa relaxation. *Physica B*, 289-290:594–597, 2000.

- 
- [55] R.H. Heffner. Muon spin depolarization in nonmagnetic metals doped with paramagnetic impurities. *Hyperfine Interact.*, 8:655–662, 1981.
- [56] J.A. Brown *et al.* Muon Depolarization by Paramagnetic Impurities in Nonmagnetic Metals. *Phys. Rev. Lett.*, 47:261–264, 1981.
- [57] B. Jamieson. *Measurement of the muon decay asymmetry parameter with the TWIST spectrometer.* PhD thesis, University of British Columbia, 2006.
- [58] T.D. Lee and C.N. Yang. Question of Parity Conservation in Weak Interactions. *Phys. Rev.*, 104(1):254–258, Oct 1956.
- [59] ARGUS collaboration. Determination of the Michel Parameters  $\rho$ ,  $\xi$ , and  $\delta$  in  $\tau$ -Lepton Decays with  $\tau \rightarrow \rho\nu$  Tags. *Phys. Lett. B*, 431:179–187, 1998.
- [60] L3 Collaboration. Measurement of the Michel parameters and the average tau-neutrino helicity from tau decays at LEP. *Phys. Lett. B*, 438:405–416, 1998.
- [61] R. Bartoldus. Measurements of the Michel Parameters in Leptonic Tau Decays using the OPAL Detector at LEP. *Nucl. Phys. B (Proc. Suppl.)*, 76:147–157, 1999.
- [62] R.L. Garwin, L.M. Lederman and M. Weinrich. Observations of the Failure of Conservation of Parity and Charge Conjugation in Meson Decays: the Magnetic Moment of the Free Muon. *Phys. Rev.*, 105:1415, January 1957.
- [63] G. R. Lynch, J. Orear, and S. Rosendorff. Muon decay in nuclear emulsion at 25 000 gauss. *Phys. Rev.*, 120(6):2277, Dec 1960.
- [64] M. Bardon, D. Berley, and L. M. Lederman. Asymmetry parameter in muon decay. *Phys. Rev. Lett.*, 2(2):56–57, Jan 1959.
- [65] Richard J. Plano. Momentum and asymmetry spectrum of  $\mu$ -meson decay. *Phys. Rev.*, 119(4):1400–1408, Aug 1960.
- [66] Akhmanov *et al.* *Sov. J. Nucl. Phys*, 6:230, 1968.
- [67] I. Beltrami *et al.* Muon decay: Measurement of the integral asymmetry parameter. *Phys. Lett. B*, 194(2):326–330, 1987.
- [68] Ali-Zade *et al.* *Soviet Phys.-JETP*, 36 (9):940, 1959.

- [69] R.S. Hayano *et al.* Search for Right-Handed Currents in the Decay  $K^+ \rightarrow \mu^+\nu$ . *Phys. Rev. Lett.*, 52(5):329–332, Jan 1984.
- [70] J. Imazato *et al.* Search for right-handed currents in the decay chain  $K^+ \rightarrow \mu^+\nu$ ,  $\mu^+ \rightarrow e + \nu\bar{\nu}$ . *Phys. Rev. Lett.*, 69(6):877–880, Aug 1992.
- [71] T. Yamanaka *et al.* Search for right-handed currents in the decay  $K^+ \rightarrow \mu^+\nu$ . *Phys. Rev. D*, 34(1):85–96, Jul 1986.
- [72] C.A. Coombes *et al.* Polarization of  $\mu^+$  Mesons from the Decay of  $K^+$  Mesons. *Phys. Rev.*, 108(5):1348–1351, Dec 1957.
- [73] D. Cutts, T. Elioff, and R. Stiening. Muon Polarization and Energy Spectrum in  $K^+ \rightarrow \pi^0 + \mu^+ + \nu$ . *Phys. Rev.*, 138(4B):B969–B979, May 1965.
- [74] D. Cutts, R. Stiening, C. Wiegand, and M. Deutsch. Measurement of the Muon Polarization Vector in  $K^+ \rightarrow \pi^0 + \mu^+ + \nu$ . *Phys. Rev.*, 184(5):1380–1392, Aug 1969.
- [75] R.S. Henderson *et al.* Precision planar drift chambers and cradle for the TWIST muon decay spectrometer. *Nucl. Instrum. Methods Phys. Res., Sect. A*, 548:306–335, August 2005.
- [76] J. Hu *et al.* Time expansion chamber system for characterization of TWIST low-energy muon beams. *Nucl. Instrum. Methods Phys. Res., Sect. A*, 566:563–574, October 2006.
- [77] C.J. Oram, J.B. Warren and G.M. Marshall. Commissioning of a new low energy  $\pi - \mu$  channel at TRIUMF. *Nucl. Instrum. Methods*, 179:95–103, January 1981.
- [78] J. Doornbos. The tuning of M13 for TWIST, theory and some results. Internal TWIST bulletin boards, December 2000.
- [79] A. Hillairet. *Measurement of  $\delta$  (in preparation)*. PhD thesis, University of Victoria, 2010.
- [80] R.E. Mischke, TRIUMF, Vancouver, Canada. Private communication.
- [81] T. Prokscha *et al.* The new  $\mu$ E4 beam at PSI: A hybrid-type large acceptance channel for the generation of a high intensity surface-muon beam. *Nucl. Instrum. Methods Phys. Res., Sect. A*, 595.

- 
- [82] J.E. Draper. Beam Steering with Quadrupole and with Rectangular Box Magnets. *Rev. Sci. Instrum.*, 37:1390, October 1966.
- [83] R.P. MacDonald. *A Precision Measurement of the Muon Decay Parameters  $\rho$  and  $\delta$* . PhD thesis, University of Alberta, 2008.
- [84] J. Musser. *Measurement of the Michel parameter  $\rho$  in muon decay*. PhD thesis, Texas A&M University, 2005.
- [85] Vector Fields. OPERA 3D simulation software. <http://vectorfields.com>.
- [86] A. Gaponenko. *A Precision Measurement of the Muon Decay Parameter  $\delta$* . PhD thesis, University of Alberta, 2005.
- [87] D. Wright. TN1: DME / He WC Gas Comparison. Technical report, TWIST collaboration, TRIUMF, October 1996.
- [88] R. Openshaw, TRIUMF, Vancouver, Canada. Private communication.
- [89] LeCroy Corporation. 1877 Multihit Time-to-Digital Converter: Specification. <http://www.lecroy.com/lrs/dsheets/1877.htm>.
- [90] LeCroy Corporation. LeCroy 1877 Fastbus TDC Manual.
- [91] R. Brun and F. Rademakers. ROOT - An Object Oriented Data Analysis Framework. *Nucl. Inst. & Meth. in Phys. Res. A*, 389:81–86, 1997.
- [92] CERN Application Software Group. GEANT Detector Description and Simulation Tool, Version 3.21, 1994.
- [93] F. James. Fitting tracks in wire chambers using the Chebyshev norm instead of least squares. *Nucl. Instrum. Methods Phys. Res.*, 211(1):145 – 152, 1983.
- [94] R. Veenhof. Garfield - simulation of gaseous detectors. CERN Program Library W5050.
- [95] P. Depommier. TN49: Muon polarisation in electromagnetic fields. Technical report, TWIST collaboration, TRIUMF, 2001.
- [96] P. Gumplinger, TRIUMF, Vancouver, Canada. Private communication.

- [97] R. Bayes. *Measurement of  $\rho$  (in preparation)*. PhD thesis, University of Victoria, 2010.
- [98] G.M. Marshall, TRIUMF, Vancouver, Canada. Private communication.
- [99] R. Armenta. TN68: TWIST Magnet: Field Map Study. Technical report, TWIST collaboration, TRIUMF, 2002.
- [100] M. Simard. Study of the Magnetic Field Map for TWIST at TRIUMF. Technical report, TWIST collaboration, TRIUMF, 2003.
- [101] C. Boucher-Veronneau. The TWIST Solenoid Magnetic Field. Technical report, TWIST collaboration, TRIUMF, 2004.
- [102] S. Fotooshi. Modeling the TWIST Magnet. Technical report, TWIST collaboration, TRIUMF, 2005.
- [103] A. Grossheim, TRIUMF, Vancouver, Canada. Private communication.
- [104] G. Marshall. OPERA map corrections from Hall and NMR maps at 2.0 T. Internal TWIST report, April 2009.
- [105] COMSOL. COMSOL Multiphysics. <http://www.comsol.com>.
- [106] V. Selivanov. TN65: GARFIELD Simulation of the TEC. Technical report, TWIST collaboration, TRIUMF, 2002.
- [107] V. Selivanov. TN65.4: One dimension TEC at  $B = 2$  T. Technical report, TWIST collaboration, TRIUMF, 2004.
- [108] P. Depommier. TN96: Muon polarization in the  $\pi^+ \rightarrow \mu^+ \nu \gamma$  decay. Technical report, TWIST collaboration, TRIUMF, 2005.
- [109] A. Grossheim *et al.* Decay of negative muons bound in  $^{27}\text{Al}$ . *Phys. Rev. D*, 80(5):052012, Sep 2009.
- [110] H. Yukawa. On the Interaction of Elementary Particles. *I*, *Proc. Phys.-Math. Soc. Jpn.*, 17:48, 1935.
- [111] C.D. Anderson and S.H. Neddermeyer. Cloud Chamber Observations of Cosmic Rays at 4300 Meters Elevation and Near Sea-Level. *Phys. Rev.*, 50:263–271, 1936.

- 
- [112] S.H. Neddermeyer and C.D. Anderson. Cosmic-Ray Particles of Intermediate Mass. *Phys. Rev.*, 54:88–89, 1938.
- [113] S.H. Neddermeyer and C.D. Anderson. Nature of Cosmic-Ray Particles. *Rev. Mod. Phys.*, 11:191–207, 1939.
- [114] M. Riordan. *The Hunting of the Quark*. Sage Publications, 1987.
- [115] M. Conversi, E. Pancini and O. Piccioni. On the Disintegration of Negative Mesons. *Phys. Rev.*, 71:209–210, 1947.
- [116] E. Fermi, E. Teller and V. Weisskopf. The Decay of Negative Mesotrons in Matter. *Phys. Rev.*, 71:314–315, 1947.
- [117] C.M.G. Lattes, G.P.S. Occhialini and C.F. Powell. Observations on the Tracks of Slow Mesons in Photographic Emulsions Part 1. *Nature*, 160:453–456, 1947.
- [118] C.M.G. Lattes, G.P.S. Occhialini and C.F. Powell. Observations on the Tracks of Slow Mesons in Photographic Emulsions Part 2. *Nature*, 160:486–492, 1947.
- [119] T.D. Lee. A Brief History of the Muon. *Hyperfine Interact.*, 86:439–453, 1994.
- [120] C.S. Wu and V.W. Hughes. *Muon Physics: Introduction and History*. Academic Press Inc., 1977.
- [121] R.A. Millikan. Mesotron as the Name of the New Particle. *Phys. Rev.*, 1:105, December 1938.
- [122] C.D. Anderson and S.H. Neddermeyer. Mesotron (Intermediate Particle) as a Name for the New Particles of Intermediate Mass. *Nature*, 142:878, November 1938.
- [123] H. Lyle. Anderson, Carl. Interview by Harriett Lyle. Oral History Project, California Institute of Technology. Retrieved April 2008 from the World Wide Web: [http://resolver.caltech.edu/CaltechOH:OH\\_Anderson\\_C](http://resolver.caltech.edu/CaltechOH:OH_Anderson_C), 1979.
- [124] A.H. Compton. Foreword: Symposium on Cosmic Rays. *Rev. Mod. Phys.*, 11:122, 1939.
- [125] H.J. Bhabha. The Fundamental Length Introduced by the Theory of the Mesotron (Meson). *Nature*, 143:276–277, February 1939.

- [126] J. L. Beveridge *et al.* A spin rotator for surface  $\mu^+$  beams on the new M20 muon channel at TRIUMF. *Nucl. Instrum. Methods Phys. Res., Sect. A*, 240:316–322, 1985.
- [127] Triumf CMMS. Helios superconducting solenoid. Website: <http://cmms.triumf.ca/equip/helios.html>.
- [128] G. Morris, TRIUMF, Vancouver, Canada. Private communication.
- [129] S.R. Dunsiger *et al.* Magnetic field dependence of muon spin relaxation in geometrically frustrated  $\text{Gd}_2\text{Ti}_2\text{O}_7$ . *Phys. Rev. B*, 73(172418), 2006.
- [130] F. James. MINUIT – Function Minimization and Error Analysis, CERN Program Library Entry D 506.
- [131] J.F. Ziegler. The stopping and range of ions in matter. <http://www.srim.org/>.
- [132] TRIUMF CS. TRIUMF Computing Services description of SRIM. <http://it-services.triumf.ca/scientific-computing/software/detector-engineering/srim-1>.
- [133] D.M. Garner. *Application of the muonium spin rotation technique to a study of the gas phase chemical kinetic of muonium reactions with the halogens and hydrogen halides*. PhD thesis, University of British Columbia, June 1979.
- [134] J. Doornbos, TRIUMF, Vancouver, Canada. Private communication.